

Direct cytosolic delivery of siRNA via cell membrane fusion using cholesterol-enriched exosomes

Received: 8 October 2023

Accepted: 8 August 2024

Published online: 19 September 2024

 Check for updates

Yan Zhuo^{1,2,8}, Zhen Luo^{3,8}, Zhu Zhu^{1,4}, Jie Wang^{1,5}, Xiang Li^{1,6}, Zhuan Zhang¹, Cong Guo^{1,6}, Bingqi Wang^{1,6}, Di Nie^{1,6}, Yong Gan^{1,6,7}✉, Guoqing Hu^{1,6}✉ & Miaorong Yu^{1,6}✉

Efficient cytosolic delivery is a significant hurdle when using short interfering RNA (siRNA) in therapeutic applications. Here we show that cholesterol-rich exosomes are prone to entering cancer cells through membrane fusion, achieving direct cytosolic delivery of siRNA. Molecular dynamics simulations suggest that deformation and increased contact with the target cell membrane facilitate membrane fusion. In vitro we show that cholesterol-enriched milk-derived exosomes (MEs) achieve a significantly higher gene silencing effect of siRNA, inducing superior cancer cell apoptosis compared with the native and cholesterol-depleted MEs, as well as conventional transfection agents. When administered orally or intravenously to mice bearing orthotopic or subcutaneous tumours, the cholesterol-enriched MEs/siRNA exhibit antitumour activity superior to that of lipid nanoparticles. Collectively, by modulating the cholesterol content of exosome membranes to facilitate cell entry via membrane fusion, we provide a promising approach for siRNA-based gene therapy, paving the way for effective, safe and simple gene therapy strategies.

RNA interference (RNAi) is a powerful mechanism for silencing specific genes using small RNA molecules^{1,2}, such as small interfering RNA (siRNA). SiRNA can be synthetically designed to target and degrade complementary messenger RNAs, effectively suppressing the translation of specific proteins³. This strategy holds immense promise for treating various diseases, including genetic disorders and cancers^{4,5}. To harness the therapeutic potential of RNAi, researchers have explored nanoparticles to deliver siRNA molecules^{6–8}. Nanoparticles, often composed of lipids, polymers or other materials, protect siRNA from degradation in the bloodstream, enhance cellular uptake and facilitate lysosomal escape^{9–11}. However, nanoparticle-based siRNA delivery

systems face significant challenges, particularly in achieving efficient cytosolic release and avoiding immunogenic responses^{12–14}. Leading nanoparticles, such as lipid nanoparticles (LNPs), facilitate siRNA release into the cytoplasm at a limited rate of only 1–4%^{15–17}. Furthermore, nanoparticle-mediated siRNA delivery often relies on the ‘proton sponge’ effect, which can inadvertently trigger lysosomal disruption, causing cellular toxicity and inflammation^{18,19}. Therefore, innovative strategies are needed to surmount these limitations and fully unlock the therapeutic potential of nanoparticle-mediated siRNA delivery.

Compared with synthetic nanoparticles, exosomes, which are nanosized extracellular vesicles, serve as more biocompatible delivery

¹State Key Laboratory of Drug Research and Center of Pharmaceutics, Shanghai Institute of Materia Medica, Chinese Academy of Sciences, Shanghai, China. ²School of Pharmacy, Jiangxi Medical College, Nanchang University, Nanchang, China. ³Department of Engineering Mechanics, State Key Laboratory of Fluid Power and Mechatronic Systems, Zhejiang University, Hangzhou, China. ⁴School of Pharmacy, Henan University, Kaifeng, China. ⁵School of Pharmacy, Shanghai University of Traditional Chinese Medicine, Shanghai, China. ⁶University of Chinese Academy of Sciences, Beijing, China. ⁷NMPA Key Laboratory of Quality Research and Evaluation of Pharmaceutical Excipients, National Institutes for Food and Drug Control, Beijing, China. ⁸These authors contributed equally: Yan Zhuo, Zhen Luo. ✉e-mail: ygan@simmm.ac.cn; ghu@zju.edu.cn; mryu@simmm.ac.cn

vehicles²⁰. Exosomes, derived from various sources, offer promising features for siRNA delivery, including prolonged circulation, inherent tissue targeting ability, low toxicity and minimal immunogenicity^{21,22}. Unfortunately, exosomes primarily enter cells via endocytosis, followed by the entrapment within endolysosomal compartments^{23,24}. This results in the degradation of encapsulated siRNA in the acidic and enzymatic endolysosomal environment, which significantly compromises delivery efficacy²⁵. By contrast, natural vesicular structures, such as enveloped viruses and synaptic vesicles, have evolved mechanisms to directly introduce cargo into the cellular cytosol through membrane fusion^{26,27}, bypassing endosomal entrapment and optimizing transportation efficiency^{28–31}. Evidence underscores that the membranes of enveloped viruses and synaptic vesicles possess a high cholesterol content, which is essential for the fusion process with cell membranes^{32–36}. Inspired by these observations, we hypothesized that cholesterol could potentially modulate the interaction between exosomes and cells, and that supplementing exosome membranes with additional cholesterol could redirect their internalization pathways towards membrane fusion.

In this study, we show theoretically and experimentally that increasing the membrane cholesterol content of exosomes enabled their entry into cells via membrane fusion with the cell membrane, contributing to efficient and safe delivery of siRNA. Specifically, this phenomenon was observed in various exosome types, including cholesterol-incorporated exosomes derived from milk (referred to as milk-derived exosomes (MEs)) and ginger (referred to as ginger-derived exosomes (GEs)), as well as naturally cholesterol-rich exosomes derived from human liver cancer cell HepG2 (HepG2-derived exosomes). Molecular dynamics (MD) simulations revealed that exosomes rich in membrane cholesterol underwent deformation, increasing their contact area with the cell membrane and ultimately resulting in membrane fusion. We further investigated MEs *in vitro* and *in vivo*. At the cellular level, siPLK1-loaded exosomes with 30% cholesterol modification (30%Chol/MEs) effectively suppressed PLK1 mRNA and protein expression, outperforming positive controls Lipofectamine 2000 and RNAiMAX in inducing tumour cell apoptosis. We then validated the *in vivo* efficacy of 30%Chol-MEs/siPLK1 through oral administration and intravenous injection, demonstrating their effective inhibition of *in situ* and ectopic colorectal tumour growth.

MD simulations of exosome–cell membrane interaction

Our initial coarse-grained molecular dynamics (CGMD) simulations were designed to determine whether increasing the cholesterol content of exosomes could improve the delivery of therapeutic agents to cells via membrane fusion. Figure 1a depicts the molecular structure of the exosomes consisting of fixed amounts of 1,2-dioleoyl-*sn*-glycero-3-*p* phosphocholine (DOPC), dioleoylphosphatidylethanolamine (DOPE) and stearyl-sphingomyelin (DPSM) molecules, but varying numbers of cholesterol molecules. The simulations revealed a gradual thickening of the exosome membrane with increased cholesterol. As captured in the snapshots in Fig. 1b, a distinct dichotomy emerged in the interaction patterns of exosomes and cell membranes, where those with lower cholesterol concentrations (0% and 11%) primarily underwent endocytosis, whereas those with higher concentrations (23% and 30%) tended to fuse with cell membranes. This divergence in interaction modes can be better understood by analysing the radial distortion function (RDF) of DOPC, which is the most abundant lipid in exosomes (Fig. 1c). The RDF patterns for exosomes containing either 0% or 11% cholesterol confirmed the structural integrity characteristic of endocytosis. However, for exosomes with elevated cholesterol levels, particularly 23% and 30%, the RDF illustrated a more dispersed distribution. The dispersion indicates that DOPC molecules migrated from the exosomes and fused with cell membranes. In parallel, cholesterol molecules also migrated from the exosomes, underwent a transitional fusion phase and finally integrated into the cell membrane.

Figure 1d presents a detailed visual examination of the fusion event, providing a magnified view of the interaction between a cell membrane and an exosome with 30% cholesterol. The sequence begins with transient lipid fluctuations and localized perturbations in lipid bilayer integrity that precede the formation of a stable pore. In particular, small perturbations in the lipid packing induced by thermal movements can lead to transient nanopore formations. These formations do not always evolve into stable pores, but can act as nucleation sites for pore formation under certain conditions, such as the presence of cholesterol. At the first point of contact between the exosome and the cell membrane, a miniscule pore forms in areas of positive curvature (0.2 μs). Following this initial pore, cholesterol plays a critical role in stabilizing the pore structure, allowing more efficient lipid exchange. This stabilization is attributed to cholesterol's ability to wedge itself between lipids, thereby increasing membrane curvature and flexibility. In addition, cholesterol molecules can escape from the exosome through the pore (0.5 μs) owing to their shorter and stiffer structure. As more cholesterol molecules integrate into the cell membrane, other lipids also follow, allowing the exosome to fuse with the cell membrane (1.0 μs).

The pivotal role of cholesterol as a stimulator in the fusion process is evident when examining the energetic parameters. The free energy curves representing the potential of mean force involved in extracting a DOPC molecule from exosomes with different cholesterol concentrations into solution are shown in Fig. 1e and Supplementary Fig. 1a. These values, although relative, provide a comparative analysis of the energetic landscape, highlighting in particular the effect of cholesterol within the exosomal membrane. The notable decrease in energy barriers in the presence of cholesterol, with a significant value of 125 kJ mol^{-1} , underscores its facilitating role in lipid exchange and fusion. Figure 1f and Supplementary Fig. 1b illustrate the translocation of DOPC and cholesterol molecules, respectively, across the cell membrane. Initially, both molecules exhibit negative free energies, suggesting spontaneous fusion. Upon the application of an external force, these energies become positive, indicating that DOPC molecules encounter a higher energy barrier than cholesterol during detachment from the membrane.

Further investigation was conducted to determine if higher cholesterol concentrations would similarly enhance exosome fusion with multi-component membranes. Fusion was consistently observed at 30% cholesterol, as shown in Fig. 1g,h. A key variable in the simulations was the modulation of cell membrane surface tension, which included conditions of constant low (0 bar), constant high (4 bar) and progressively increasing tension (from 0 bar to 4 bar). Importantly, exosomes containing 30% cholesterol successfully fused with multi-component membranes under all surface tension scenarios. In particular, higher surface tensions leading to less dense lipid arrangements seemed to facilitate the fusion process. This is supported by increased cholesterol diffusion and higher interaction energy (in absolute terms) between the exosome and the membrane, as shown in Fig. 1i.

Preparation and characterization of Chol/MEs

To investigate cholesterol's effect on exosome–cell interaction, we first engineered MEs with different cholesterol levels. The native MEs had approximately 18% cholesterol (w%). To alter the cholesterol content, we used methyl- β -cyclodextrin (Me β CD) to extract cholesterol from the ME membrane or introduced cholesterol into the ME membrane via a film hydration method (Fig. 2a), resulting in engineered ME membranes with cholesterol contents of approximately 5% (w%), 10% (w%), 23% (w%) and 30% (w%) (Fig. 2b). These engineered MEs exhibited particle sizes around 140 nm and zeta potentials of -12 mV (Fig. 2c). Transmission electron microscopy (TEM) showed cup-shaped morphology of MEs diminished concomitantly as the membrane cholesterol content increased (Fig. 2d), likely owing to cholesterol's ability to stabilize and thicken lipid membranes. Furthermore, atomic force microscopy (AFM) analysis

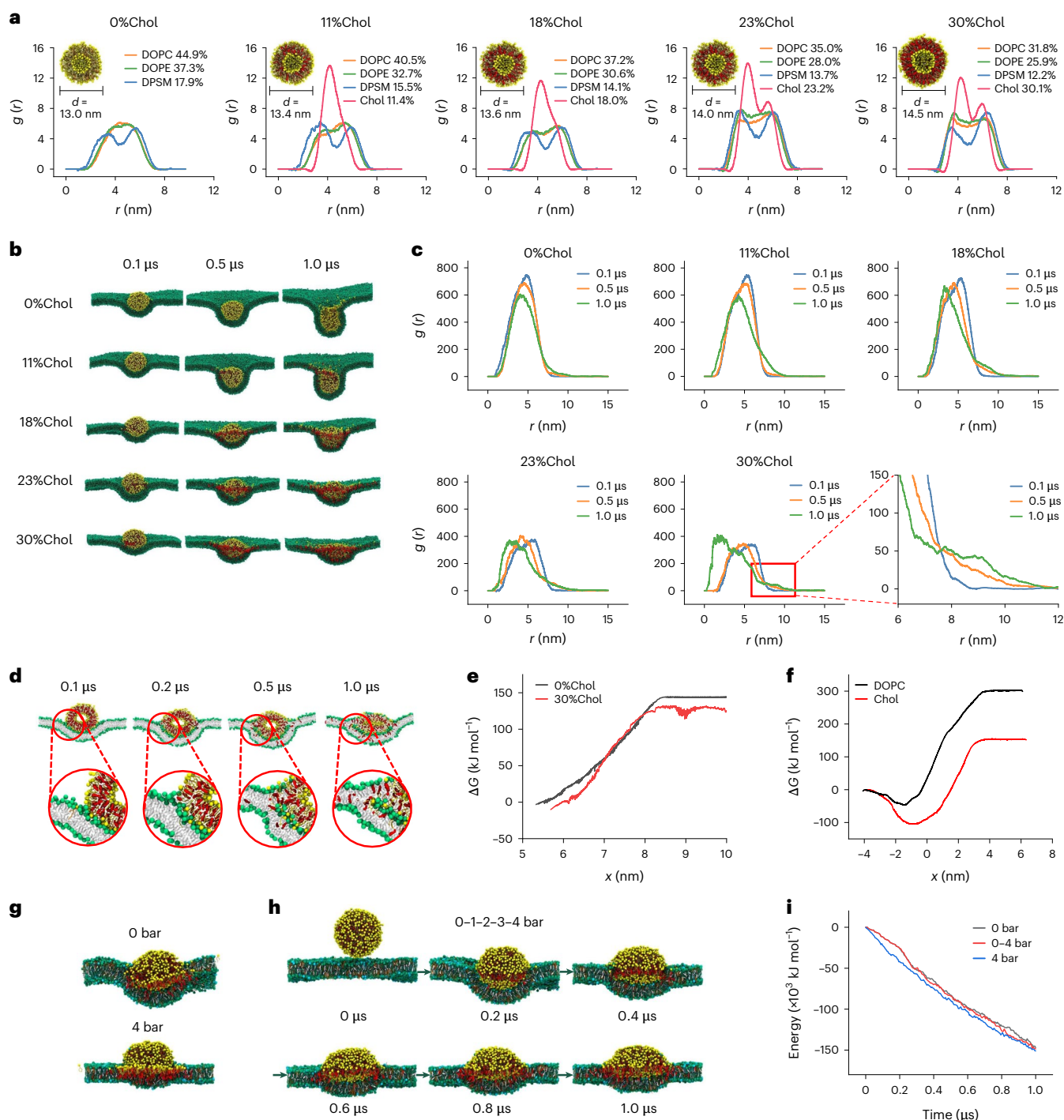


Fig. 1 | The CGMD simulations of effects of cholesterol concentration on the interactions between exosomes and cell membranes. **a**, Molecular structure representation of exosomes composed of DOPC, DOPE and DPSM with different amounts of cholesterol, highlighting the increase in membrane thickness of exosomes with increasing cholesterol concentration. **b**, Snapshots depicting the interaction between exosomes and cell membranes, showing the dichotomy based on cholesterol content concentrations: endocytosis in exosomes with 0% and 11% cholesterol and fusion at higher cholesterol concentrations (23% and 30%). **c**, RDF of DOPC at 0.1 μ s, 0.5 μ s and 1.0 μ s showing structural integrity in exosomes with 0% and 11% cholesterol and dispersed distribution with higher cholesterol, illustrating the tendency of MEs to fuse with cell membranes. **d**, Detailed visualization of fusion between 30% cholesterol exosome and a cell membrane, tracking from initial pore formation (0.2 μ s) to fusion (1.0 μ s). **e**, Free energy analysis showing that the exosome with higher cholesterol incorporation requires less energy to release DOPC molecules than that without

cholesterol. **f**, Free energy changes of DOPC and cholesterol molecules crossing the POPC cell membrane showing the higher propensity of cholesterol to cross cell membranes compared with DOPC. **g**, Snapshots depicting the fusion between exosomes with 30% cholesterol and complex cell membranes under constant low tension (0 bar) and constant high tension (4 bar). **h**, Trajectory plots illustrating the fusion process as surface tension progressively increases from 0 bar to 4 bar. These visualizations show the consistency of the fusion tendencies regardless of the surface tensions of cell membranes. Cholesterol in the complex cell membrane is depicted in white, and all other lipid molecules are depicted in green. **i**, Interaction energy between exosomes and multi-component cell membranes, showing that higher tensions promote fusion. Cholesterols are shown as red rods inside exosomes and white rods inside cell membranes. DOPC (yellow), DOPE (apricot), DPSM (orange), POPC (green) and POPE (cyan) show their hydrophobic tails as rods, while only DOPC and POPC show their hydrophilic heads as beads.

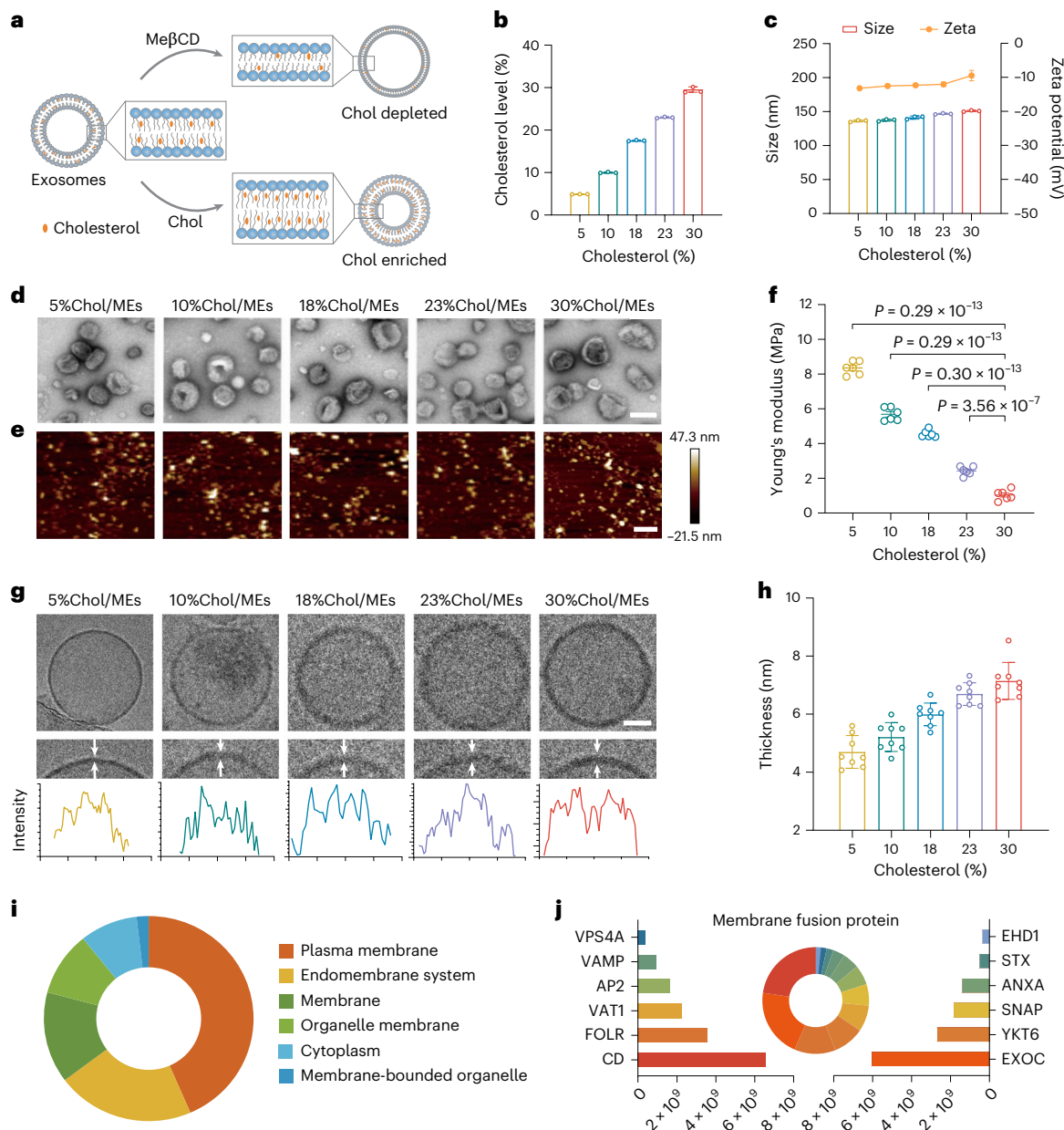


Fig. 2 | Characterization of MEs with varying cholesterol incorporation.

a, Schematics denoting the preparation of MEs with varying cholesterol incorporation. The cholesterol content in the membrane of MEs was decreased or increased by treating MEs with Me β CD or cholesterol, respectively. **b**, The cholesterol content in ME membranes detected by the Amplex Red cholesterol assay ($n = 3$ independent experiments). **c**, The hydrodynamic diameter and zeta potential of different MEs ($n = 3$ independent experiments). **d**, TEM images of different MEs. Scale bar, 100 nm. **e**, AFM images of different MEs under fluid conditions. Scale bar, 400 nm. **f**, Young's modulus values of different MEs, as

measured by AFM ($n = 6$ independent experiments). **g**, Cryo-TEM images of different MEs. Scale bar, 25 nm. **h**, The membrane thickness of different MEs ($n = 8$ replicates). **i**, Proteomics analysis of MEs. The identified proteins were classified according to their cellular components. **j**, Content and categories of proteins in the MEs involved in membrane fusion. All values are expressed as mean \pm s.d. Statistical significance was determined using ordinary one-way ANOVA with multiple comparisons in **f**. * $P < 0.05$, ** $P < 0.01$, *** $P < 0.001$, **** $P < 0.0001$.

under fluid conditions indicated that all the MEs were in spherical shape with good monodispersity (Fig. 2e).

To confirm the different cholesterol incorporation of MEs is necessary for subsequent biological evaluation. First, as cholesterol could modulate the elasticity of membrane vesicles, we conducted a quantitative evaluation of ME elasticity by using AFM. The elasticity of engineered MEs exhibited a direct correlation with the cholesterol concentration within the membrane, and a significant reduction in rigidity alongside an increase in cholesterol content on the ME membrane, causing a transition from the magnitude within the MPa range to the kPa

range (Fig. 2f). Notably, MEs with a cholesterol content of 30% showed the lowest Young's modulus (647 kPa). Second, cryo-transmission electron microscopy (cryo-TEM) investigations verified a membrane thickness change in the engineered MEs, aligning with simulated results (Fig. 2g,h). Third, we examined the protein components in the MEs by western blotting³⁷ and proteomic analysis, respectively. The three protein markers of MEs, including CD63, TSG101 and Alix, remained in the different engineered MEs (Supplementary Fig. 2). Meanwhile, a comprehensive analysis of cellular components at the genome-wide scale by proteomic analysis unveiled that the protein composition of

MEs predominantly correlated with cellular membrane structures (Fig. 2i). Notably, proteins with potential functional involvement in membrane fusion, including CD, EXOC, FOLR and SNAP proteins, exhibited statistically significant correlations (Fig. 2j). Collectively, these above-mentioned evidences demonstrated that MEs with varying cholesterol incorporation (ranging from 5% to 30%) were successfully prepared.

The encapsulation efficiency (EE) and loading capacity (LC) of engineered MEs were investigated using scrambled siRNA as a model drug. siRNA was efficiently loaded into engineered MEs by electroporation, with EE of approximately 75% and LC around 4.0% (Supplementary Fig. 3 and Supplementary Table 1). In addition, we verified the good safety and stability of the engineered MEs (Supplementary Figs. 4 and 5), suggesting that the engineered MEs would be a safe and stable delivery system for in vivo applications.

Chol-enriched MEs enter cancer cells via membrane fusion

Next, we investigated the cellular uptake capacity of engineered MEs. Evidently, the confocal laser scanning microscopy (CLSM) results and the flow cytometry analysis showed that the uptake of MEs by human colorectal cancer cells (HCT116 cells) increased with an increase in membrane cholesterol (Supplementary Fig. 6a,b). Specifically, 30%Chol/MEs showed 4.0-, 3.5-, 2.0- and 1.6-fold enhancement in uptake compared with 5%Chol/MEs, 10%Chol/MEs, 18%Chol/MEs and 23%Chol/MEs, respectively (Supplementary Fig. 6c).

Previous studies have proved that different cellular uptake mechanisms can lead to different uptake efficiencies, and fusion, compared with the high-energy-dependent endocytosis pathway, is a low energy cost pathway, which could facilitate cellular uptake^{38,39}. We thus assumed that the cholesterol-enriched MEs might be internalized by HCT116 cells via membrane fusion. To validate this hypothesis, the CLSM observations revealed that the red signals of 30%Chol/MEs were almost overlapped with the green signals of the cell membrane (Fig. 3a), indicating that 30%Chol/MEs could fuse with the cancer cell membrane. By contrast, no apparent colocalization was found in the native MEs and cholesterol-depleted MEs groups (Fig. 3a). In addition, the membrane fusion process was monitored in real time. As shown in Fig. 3b and Supplementary Videos 1 and 2, the red signal of 30%Chol/MEs gradually merged with the cell membrane (green), indicating that 30%Chol/MEs fused with the HCT116 cell membrane. For 5%Chol/MEs, they adhered to the cell membrane followed by the vesicle entrapment, and were finally transported to the cytoplasm. For further mechanism validation, HCT116 cells were pretreated with various internalization inhibitors. As illustrated in Fig. 3c, pretreatment of cells substantially reduced the intracellular internalization of the native MEs and cholesterol-depleted MEs groups, while pretreating cells reduced the uptake of the cholesterol-enriched MEs to a lesser extent. The additional analysis of fluorescence resonance energy transfer (FRET) assay confirmed the fusion between 30%Chol/MEs and HCT116 cells (Fig. 3d,e and Supplementary Fig. 7), and the average fusion efficiency within 2 h was approximately 57.8% (Fig. 3f). TEM images further verified the membrane fusion between 30%Chol/MEs and HCT116 cells (Fig. 3g and Supplementary Fig. 8). These results indicated that the uptake of the cholesterol-enriched MEs was primarily dependent on membrane fusion.

After membrane fusion, the cholesterol-enriched MEs exhibit the potential to circumvent the endocytosis-endosome pathway, facilitating direct transport of inner cargos into the cytoplasm. Conversely, cholesterol-depleted MEs tend to be sequestered in endosomes post-endocytosis. To discriminate different intracellular trafficking pathways, we incubated MEs with cells expressing EGFP-labelled Rab5^{Q79L}, which serves as an early endosome marker. We detected internalized 5%Chol/MEs within early endosomes (Fig. 3h). By contrast, cases of 30%Chol/MEs within early endosomes were notably absent.

Concurrently, CLSM images revealed a pronounced colocalization of 5%Chol/MEs with lysosomes (Supplementary Fig. 9), underscoring the involvement of the endosome–lysosome pathway following endocytosis. To further delineate the spatial distribution, we utilized rhodamine B to label the inner water compartment of MEs, and three-dimensional (3D) imaging was performed post-incubation with HCT116 cells. Results indicated that the red fluorescence emanating from 30%Chol/MEs was uniformly dispersed throughout the entire cell (Fig. 3i and Supplementary Videos 3 and 4), indicating cytosolic delivery of the 30%Chol/MEs cargo through membrane fusion. This pattern contrasted sharply with the 5%Chol/MEs group, in which red spots were visible within the cell, indicating entrapment in intracellular compartments. The membrane fusion-mediated uptake was observed to be cholesterol levels dependent, not only for MEs but also for GEs. We also investigated the uptake pathways of GEs with different cholesterol levels, and the results indicated that the uptake of the cholesterol-enriched GEs was also primarily dependent on membrane fusion in cancer cells (Supplementary Fig. 10).

Furthermore, the cellular uptake of engineered MEs by other cancer cells, including human hepatocellular carcinoma cells (HepG2 cells), human cervical cancer cells (HeLa cells), human ovarian cancer cells (SK-OV-3 cells) and murine mammary carcinoma cells (4T1 cells), as well as normal cells, including intestinal epithelial cells (NCM460 cells), human embryonic kidney cells (293T cells) and mouse hippocampal neuronal cells (HT22 cells), was studied. Consistent with the results in HCT116 cells, the uptake of cholesterol-enriched MEs was primarily dependent on the membrane fusion pathway in HepG2, HeLa, SK-OV-3 and 4T1 cells (Supplementary Fig. 11a–d). However, we observed a different pattern in normal cells, including NCM460, 293T and HT22 cells. There was no significant colocalization between the cell membrane and the engineered MEs with increasing cholesterol incorporation (Supplementary Figs. 11e,f and 12a). All engineered MEs groups were internalized via an endocytosis-based pathway (Supplementary Figs. 11e,f and 12b). In summary, our comprehensive investigation into the cellular uptake of engineered MEs across a spectrum of cancer and normal cell lines has revealed a striking divergence in the mechanisms governing the uptake of cholesterol-enriched MEs. These observations provide meaningful insights into the nuanced cellular responses contingent upon context and shed light on potential implications for targeted therapeutic applications in the realm of cancer treatment.

Next, we synthesized liposomes with different cholesterol incorporation according to the phospholipid components in the MD simulation. The CLSM observed that with the increase of cholesterol incorporation in liposomes, the colocalization of red signals in liposomes and green signals in cell membranes increased significantly (Supplementary Fig. 13a). Further analysis using a FRET assay confirmed the facilitated fusion between 30%Chol/Lipo and HCT116 cells (Supplementary Fig. 13b). While cholesterol incorporation significantly enhanced membrane fusion efficiency, this enhancement is likely influenced by a complex interplay of additional factors and pathways. This series of experiments not only elucidates the impact of cholesterol content on the interaction between liposomes and cell membranes but also establishes a link between MD simulations and experimental results, thereby enhancing our understanding of the membrane fusion processes.

In addition, we expanded our study to include naturally occurring exosomes with varying cholesterol levels, thereby eliminating the need for engineering techniques. We utilized exosomes derived from HepG2 cells, known for their high cholesterol content (approximately 27.9%)⁴⁰, and CT26 cells, characterized by lower cholesterol levels (approximately 8.6%). Our comprehensive analysis, including CLSM and inhibitor studies, revealed distinct uptake mechanisms that correlated with membrane cholesterol content. Exosomes from HepG2 cells predominantly entered the cancer cells via membrane fusion (Supplementary Fig. 14a,b), a process facilitated by their higher

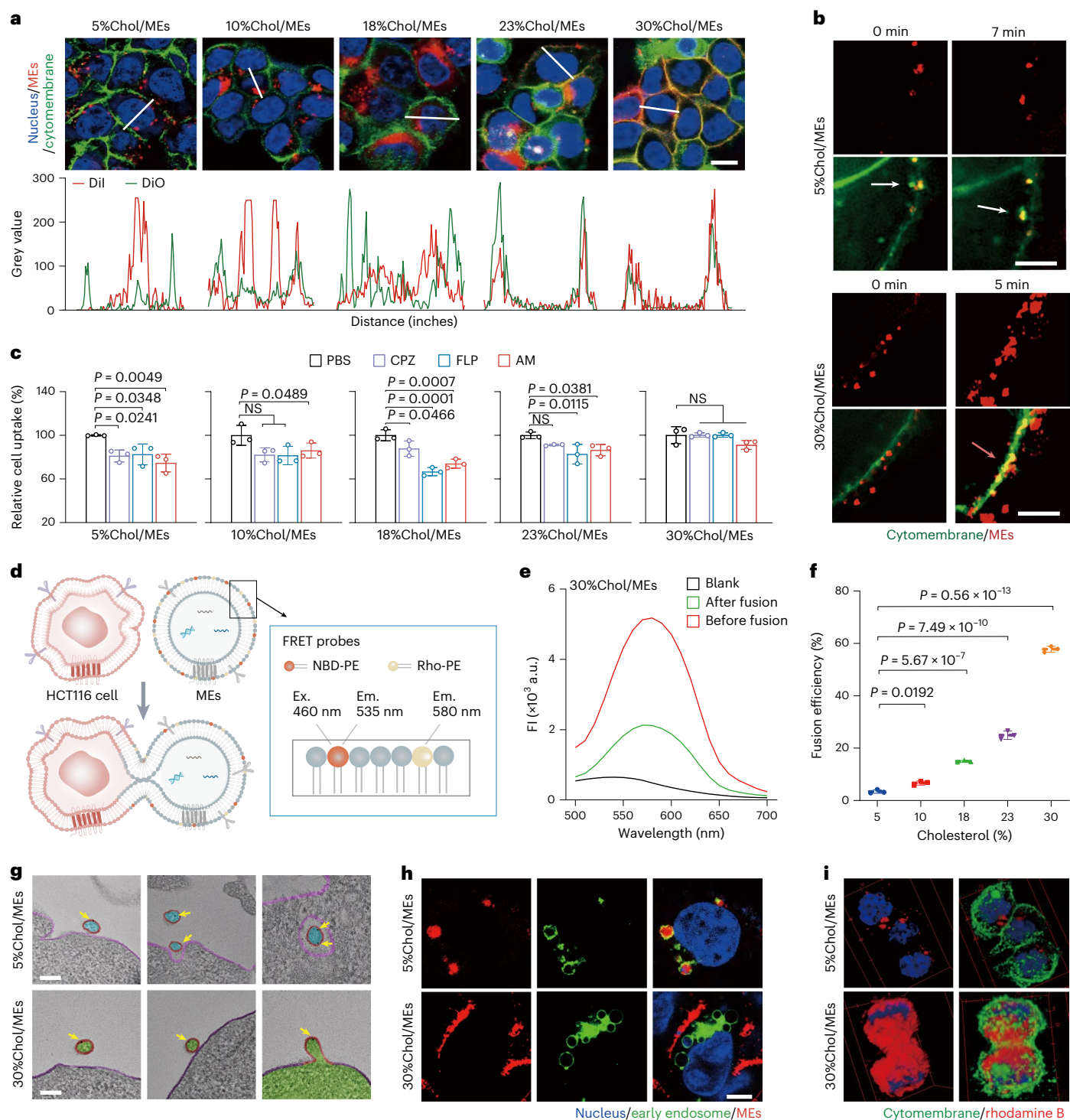


Fig. 3 MEs with varying cholesterol levels enter cells via different internalization pathways. **a**, CLSM images indicating the interaction between DiI-labelled cell membrane and DiO-labelled cell membrane and DiI-labelled MEs in HCT116 cells. Nuclei, blue; CM, green; MEs, red. Scale bar, 25 μ m. **b**, Snapshots of engineered MEs entry into HCT116 cells captured by high intelligent and sensitive structured illumination microscope (HIS-SIM). White arrows denote endocytosed MEs. Magenta arrows denote the fusion between MEs and cell membranes. DiO-labelled CM, green; DiI-labelled MEs, red. Scale bar, 5 μ m. **c**, Relative cellular uptake of engineered MEs in HCT116 cells in the presence of different endocytosis inhibitors. Chlorpromazine (CPZ, clathrin-mediated), filipin (FLP, caveolin-mediated) and amiloride (macropinocytosis-mediated endocytosis) ($n = 3$ biological independent samples). **d**, Schematic illustration of FRET assay monitoring membrane fusion between HCT116 cells and lipid dye-labelled MEs. **e**, Fusion changes emission wavelength (Em, ranged from 535 nm to 580 nm) intensity of the fluorescent

donor NBD and fluorescent acceptor rhodamine at the excitation wavelength (Ex) of 460 nm. Plotted curves indicate fusion between dye-labelled MEs and unlabelled HCT116 cells. **f**, The fusion efficiency between MEs and HCT116 cells ($n = 3$ biological independent samples). **g**, Representative Bio-TEM images of gold nanoparticle-labelled MEs-cell uptake intermediates. Outlines showing MEs (red) and cell membranes (magenta) as defined by luminal grey level distribution. Yellow arrows denote gold nanoparticle. Scale bar, 200 nm. **h**, Representative CLSM images from HCT116 cells transfected with EGFP-labelled Rabs⁵^{Q79L}. Cells were incubated with DiI-labelled MEs for 2 h. Nuclei, blue; early endosome, green; MEs, red. Scale bar, 5 μ m. **i**, 3D reconstructed confocal microscopy images of HCT116 cells after treatment with rhodamine B-loaded MEs. Nuclei, blue; CM, green; rhodamine B, red. All values are expressed as mean \pm s.d. Statistical significance was determined using ordinary one-way ANOVA with multiple comparisons in **c** and **f**. * $P < 0.05$, ** $P < 0.01$, *** $P < 0.001$, **** $P < 0.0001$, NS, not significant.

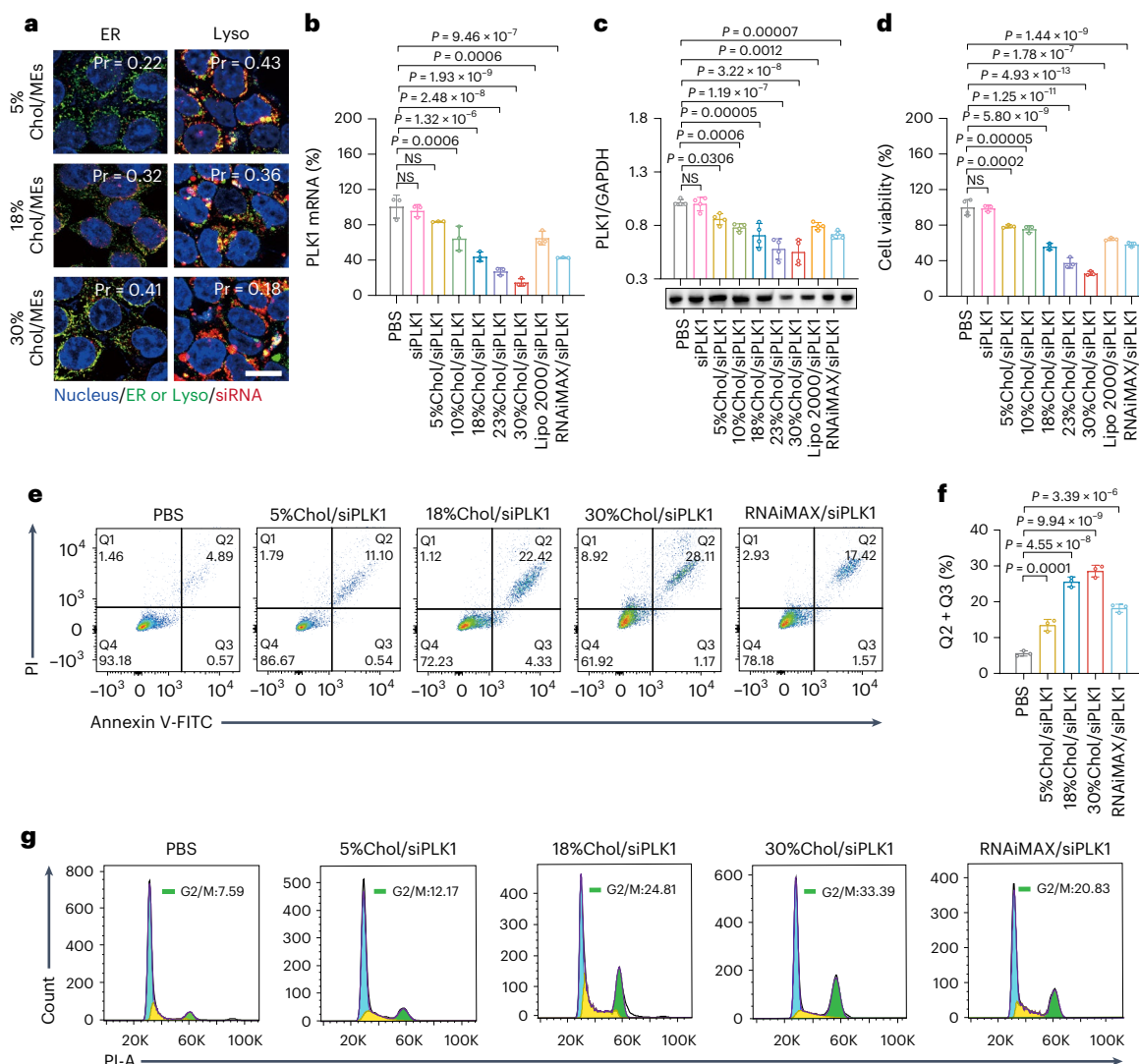


Fig. 4 | SiPLK1-loaded MEs effectively inhibited the growth of HCT116 cells in vitro. **a**, CLSM images of the colocalization of Cy3-siRNA-loaded engineered MEs with lysosomes and ER. Scale bar, 15 μ m. **b–d**, PLK1 mRNA levels by RT-qPCR (**b**), PLK1 protein expression by western blotting (**c**) and cell viability analysed by CCK-8 kit (**d**) ($n = 3$ biological independent samples). **e, f**, Examination (**e**)

and quantitative analysis (**f**) of HCT116 cell apoptosis by flow cytometry ($n = 3$ biological independent samples). **g**, Cell cycle of HCT116 cells by flow cytometry. All values are expressed as mean \pm s.d. Statistical significance was determined using ordinary one-way ANOVA with multiple comparisons in **b–d** and **f**. * $P < 0.05$, ** $P < 0.01$, *** $P < 0.001$, **** $P < 0.0001$, NS, not significant.

cholesterol content. By contrast, CT26 cell-derived exosomes, with their lower cholesterol content, were primarily internalized through endocytosis (Supplementary Fig. 14c,d). These results reinforce our earlier observations with engineered exosomes and liposomes and provide further evidence for the critical role of cholesterol in determining the cellular uptake pathway.

Chol-enriched MEs elevate siRNA gene silencing in vitro

After cellular internalization via membrane fusion, the cholesterol-enriched MEs could release loaded siRNA into the cytosol directly, thus bypassing endolysosomal entrapment. We then monitored the intracellular fates of encapsulated Cy3-siRNA. The results revealed that only a minor fraction of siRNA loaded in the 30%Chol/MEs exhibited colocalization with lysosomes, indicative of limited lysosomal entrapment. By contrast, a substantial portion of siRNA in the 5%Chol/MEs group, which entered cell via endocytosis, showed pronounced colocalization with lysosomes. Similarly, a minimal fraction of siRNA in the 5%Chol/MEs group colocalized with the endoplasmic reticulum (ER), while a considerable proportion of siRNA in the

30%Chol/MEs group showed clear colocalization with the ER (Fig. 4a and Supplementary Fig. 15). These observations imply that 30%Chol/MEs entered cells primarily through membrane fusion, efficiently releasing siRNA directly into the cytoplasm and enabling it to reach the ER for functional efficacy.

Next, we evaluated the gene silencing efficiency of siRNA-loaded MEs in HCT116 cells, using PLK1-siRNA with synthetic lethal effect as the target gene. The real-time quantitative polymerase chain reaction (RT-qPCR) results showed that the naked siPLK1-treated group had no significant change in PLK1 mRNA levels compared with the blank group. Notably, the 30%Chol/siPLK1 group showed 84.1% downregulation of PLK1 mRNA, which demonstrated a 5.3-, 2.9-, 2.4-, 1.5-, 1.5- and 1.2-fold reduction compared with 5%Chol/siPLK1, 10%Chol/siPLK1, Lipo2000/siPLK1, 18%Chol/siPLK1, RNAiMAX/siPLK1 and 23%Chol/siPLK1, respectively (Fig. 4b). Consistently, the western blotting results confirmed a significant inhibition of PLK1 protein levels of approximately 60% with 30%Chol/siPLK1 (Fig. 4c). Strikingly, 30%Chol/siPLK1 exhibited significant proliferation inhibition compared with the other siRNA-loaded formulations (Fig. 4d). Examination and quantitative analysis cell apoptosis results demonstrated that HCT116 cells treated

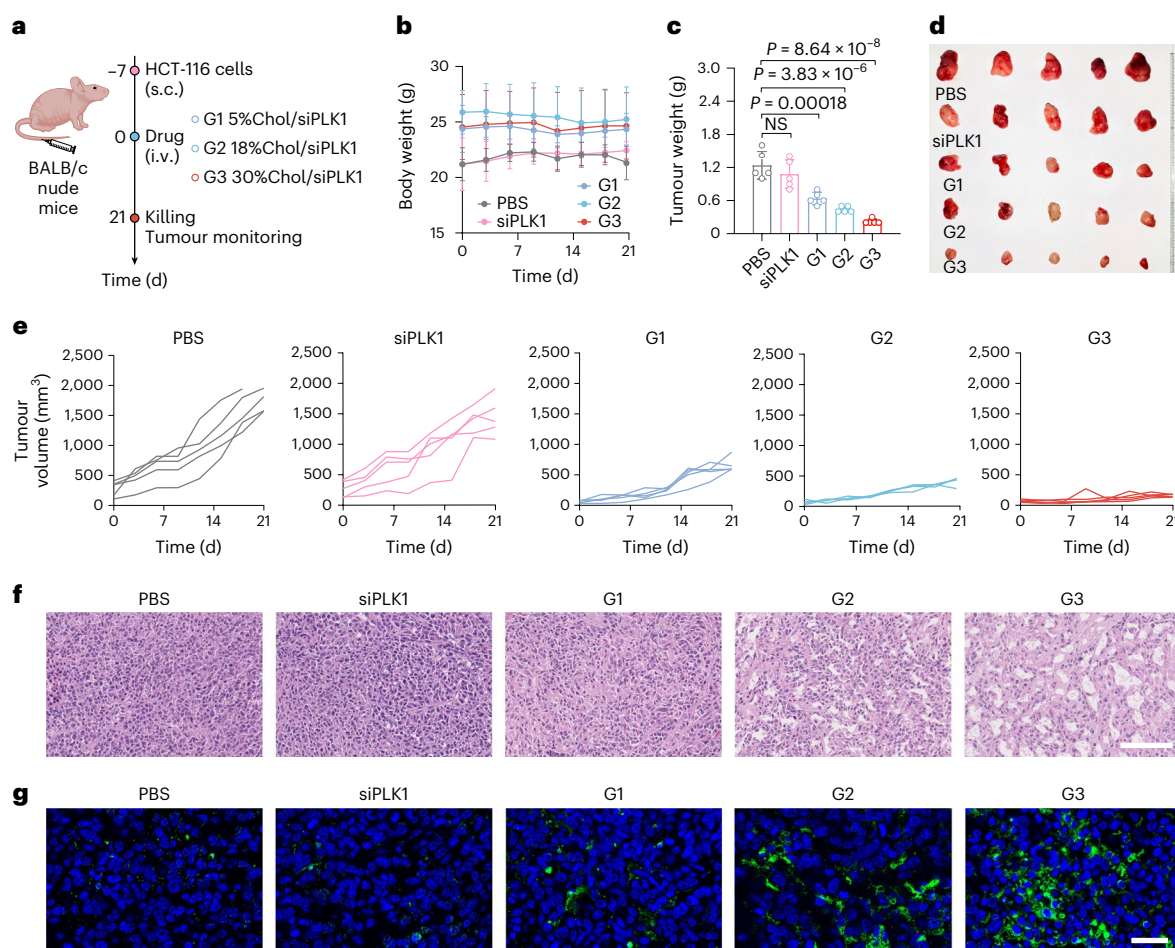


Fig. 5 | SIPLK1-loaded MEs effectively to eradicate subcutaneous HCT116 colorectal tumour-bearing mice. **a**, Scheme and grouping of in vivo therapy. The BALB/c nude mice were inoculated in subcutaneous (s.c.) with HCT116 cells (2×10^6 cells per mouse) on day -7 , and the mice were treated with engineered MEs (a siPLK1 concentration of $100 \mu\text{g kg}^{-1}$) through the tail vein (i.v.) every 3 days, over the course of 21 days. Nine groups: PBS; naked siPLK1; siPLK1/electroporation; MEs including 5%Chol/MEs, 18%Chol/MEs and 30%Chol/MEs; siRNA-loaded MEs including 5%Chol/siPLK1 (refer to G1), 18%Chol/siPLK1 (refer to G2) and 30%Chol/siPLK1 (refer to G3). **b**, Body weights of HCT116-tumour-

bearing mice recorded during treatment ($n = 5$ biological independent samples). **c**, Weights of isolated tumour tissues at the end of the experiment ($n = 5$ biological independent samples). **d**, Optical images of isolated tumour tissues at the end of the experiment. **e**, Individual tumour growth curves recorded during treatment ($n = 5$ biological independent samples). **f**, H&E staining of colonic tumour sections. Scale bar, $100 \mu\text{m}$. **g**, TUNEL staining of colonic tumour sections. Scale bar, $25 \mu\text{m}$. All values are expressed as mean \pm s.d. Statistical significance was determined using ordinary one-way ANOVA with multiple comparisons in **c**. * $P < 0.05$, ** $P < 0.01$, *** $P < 0.001$, **** $P < 0.0001$, NS, not significant.

with 30% Chol/siPLK1 exhibited an apoptotic cell population of 29.2%, including both early and late apoptotic cells (Q2 + Q3) (Fig. 4e,f and Supplementary Fig. 16a), which was significantly higher compared with RNAiMAX/siPLK1 (19.0%). In addition, we evaluated cell cycle arrest and the percentage of cells in the G2/M phase is shown in Fig. 4g and Supplementary Fig. 16b. Notably, 30%Chol/siPLK1 exhibited the highest proportion of cells in the G2/M phase. These findings suggest that 30%Chol/siPLK1 holds promise as an RNAi therapeutic platform that outperforms commercially available transfection agents.

Collectively, these findings substantiated that increasing cholesterol content on ME membranes facilitated membrane fusion-mediated cellular entry, ensuring the rapid release of siRNA into the cytoplasm. This positions 30% Chol/MEs as a promising nanoplateform for efficient siRNA delivery to cancer cells, demonstrating potent efficacy in cancer therapy.

siPLK1-loaded Chol-enriched MEs retard tumour growth

To explore the utility of siPLK1-loaded MEs for cancer treatment, we further investigated their antitumour activity in subcutaneous colorectal cancer models. The IVIS spectrum imaging system results

showed that the DiR-labelled MEs specifically targeted tumour 24 h post tail vein injection (Supplementary Fig. 17). For cancer treatment, HCT116 colorectal cancer-bearing mice were randomly divided into nine groups. Over 21 days, the different formulations were administered intravenously every 3 days (Fig. 5a). Tumour volumes and body weights were recorded. At the end, histopathological analysis of haematoxylin and eosin (H&E) staining tissue sections was performed on major organs in all groups. Remarkably, no discernible alterations were noted in terms of body weight or the histopathological constitution of tissue sections, underscoring the highly favourable safety profile of engineered MEs (Fig. 5b and Supplementary Fig. 18). Furthermore, there were no significant changes in aspartate transaminase, alanine amino transferase, tumour necrosis factor- α and interleukin-6 levels (Supplementary Fig. 19), indicating that engineered MEs have good safety and low immunogenicity in vivo.

At the end of the experiment, mice were killed and tumours were excised and weighed. The tumours treated with 30%Chol/siPLK1, 18%Chol/siPLK1 and 5%Chol/siPLK1 were approximately 7.3-, 4.1- and 2.8-fold smaller than those in the PBS group (Fig. 5c), respectively. The 30%Chol/siPLK1 group showed nearly complete tumour growth suppression (Fig. 5d). The tumours in the PBS, naked siRNA, siRNA/

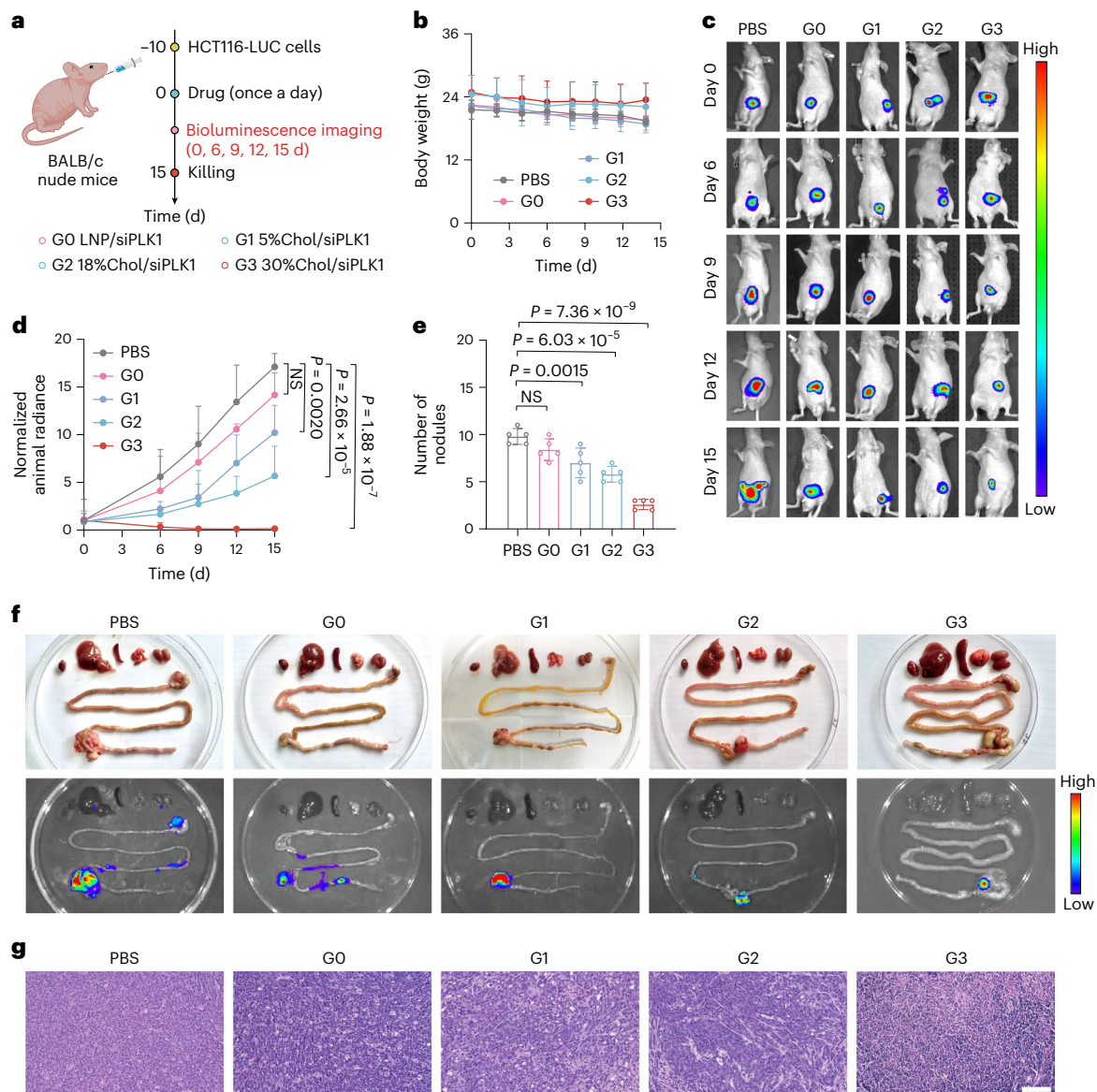


Fig. 6 | siPLK1-loaded MEs effectively to inhibit orthotopic HCT116 colorectal tumour-bearing mice. **a**, Scheme and grouping of in vivo therapy. The BALB/c nude mice were inoculated in orthotopic with HCT116-LUC cells (3×10^6 cells per mouse) on day -10, and the mice were treated with engineered MEs

(a siPLK1 concentration of $100 \mu\text{g kg}^{-1}$) through oral administration every day, over the course of 14 days. Five groups: PBS; G0, LNP/siPLK1; G1, 5%Chol/siPLK1; G2, 18%Chol/siPLK1; G3, 30%Chol/siPLK1. **b**, Body weights of tumour-bearing mice recorded during treatment ($n = 5$ biological independent samples). **c**, Representative in vivo bioluminescence imaging of the orthotopic colorectal

tumour at the indicated time. **d**, Tumour growth profiles obtained through quantifying the bioluminescence ($n = 5$ biological independent samples). **e**, The number of tumour nodules ($n = 5$ biological independent samples). **f**, Representative ex vivo photographs (upper panel) and bioluminescence imaging (lower panel) of various organs. **g**, H&E staining of colonic tumour sections. Scale bar, $100 \mu\text{m}$. All values are expressed as mean \pm s.d. Statistical significance was determined using ordinary one-way ANOVA with multiple comparisons in **b**, **d** and **e**. * $P < 0.05$, ** $P < 0.01$, *** $P < 0.001$, **** $P < 0.0001$, NS, not significant.

electroporation and MEs without siRNA groups grew rapidly, while the treatment with 5%Chol/siPLK1, 18%Chol/siPLK1 or 30%Chol/siPLK1 significantly reduced the tumour volume (Fig. 5e and Supplementary Fig. 20). The cell apoptosis was analysed by H&E staining. Tumour sections treated with naked siRNA exhibited distinct nuclei and cytoplasm, similar to the PBS group. By contrast, the 30%Chol/siPLK1 group showed signs of nuclear shrinkage and increased extracellular space, indicating enhanced tumour cell apoptosis (Fig. 5f). In addition, the terminal deoxynucleotidyl transferase dUTP nick end labelling (TUNEL) assay revealed significant DNA fragmentation within tumour cells following administration of the 30%Chol/siPLK1 group (Fig. 5g). These results demonstrate that siPLK1 could be successfully delivered to target cancer cells by the cholesterol-enriched MEs, thus efficiently

inhibited cell proliferation, induced cell apoptosis and eventually suppressed tumour progression.

To further explore the therapeutic potential of the siPLK1-loaded MEs, we established an orthotopic CRC mouse model. Mice showed comparable bioluminescence intensity of the tumours and were divided into five groups. The IVIS spectral imaging indicated that the Cy5.5-siRNA-labelled MEs were significantly colocalized with luciferase-expressing tumour cells, demonstrating that the engineered MEs could be retained in the colon and taken up by colorectal cancer cells 24 h after oral administration (Supplementary Fig. 21). Afterwards, each group of mice was given orally a preparation containing siPLK1 at $100 \mu\text{g kg}^{-1}$ every day for 14 days (Fig. 6a). During the treatment, the mice had similar weight and H&E staining of major organs in all groups

showed no significant histological toxicity compared with the control group, indicating good biocompatibility (Fig. 6b and Supplementary Fig. 22). Furthermore, bioluminescence imaging monitored tumour growth (Fig. 6c). Similar to the PBS treatment, LNP/siPLK1 did not delay tumour growth (Fig. 6d). By contrast, 5%Chol/siPLK1 and 18%Chol/siPLK1 demonstrated significant tumour growth inhibition (Fig. 6d). Notably, the tumours regressed in mice treated with 30%Chol/siPLK1, exhibiting the strongest antitumour effect (Fig. 6d).

At the end of the experiment, the mice were killed and tumours were excised. The tumours treated with 5%Chol/siPLK1, 18%Chol/siPLK1 and 30%Chol/siPLK1 were approximately 1.4-, 1.7- and 3.8-fold smaller than those in the PBS group (Fig. 6e), respectively. Notably, tumours in the PBS group metastasized to various organs (Fig. 6f), demonstrating the remarkable aggressiveness and invasiveness of this malignant tumour. However, this was not seen in the MEs/siPLK1 treatment groups, highlighting the therapeutic effect of these formulations on tumour metastasis. Furthermore, H&E staining revealed a significant decrease of colorectal cancer when PLK1 were knocked down. The tumour section treated with LNP/siPLK1 showed a well-defined nucleus and cytoplasm similar to the PBS-treated group. By contrast, the nuclear atrophy and extracellular space increment were observed in the MEs/siPLK1-treated groups, indicating the more efficient cell apoptosis in tumours (Fig. 6g). Taken together, these data indicate that PLK1 siRNA delivery by the cholesterol-enriched MEs efficiently prevented CRC growth in vivo.

Conclusion

In summary, we have made a significant step forward in the field of siRNA-based gene therapy by providing a novel and effective approach to siRNA delivery through cholesterol-enriched exosomes. By achieving membrane fusion, the cholesterol-enriched exosomes eliminate the shortcomings associated with endosomal entrapment, thereby enhancing the overall efficiency of siRNA delivery. Of note, unlike some synthetic nanoparticles and fusogenic agents, cholesterol-enriched exosomes are more biocompatible and less likely to trigger unwanted immune responses. This property is critical for the development of safe and well-tolerated gene therapy strategies. Therefore, the successful modulation of cholesterol content in exosome membranes to promote membrane fusion-mediated cargo transfer offers exciting opportunities for the development of safer and more efficient gene therapy strategies.

Online content

Any methods, additional references, Nature Portfolio reporting summaries, source data, extended data, supplementary information, acknowledgements, peer review information; details of author contributions and competing interests; and statements of data and code availability are available at <https://doi.org/10.1038/s41565-024-01785-0>.

References

- Hu, B. et al. Thermostable ionizable lipid-like nanoparticle (iLAND) for RNAi treatment of hyperlipidemia. *Sci. Adv.* **8**, eabm1418 (2022).
- Zhao, J. H. & Guo, H. S. RNA silencing: from discovery and elucidation to application and perspectives. *J. Integr. Plant Biol.* **64**, 476–498 (2022).
- Chen, Y. et al. Targeting Xkr8 via nanoparticle-mediated in situ co-delivery of siRNA and chemotherapy drugs for cancer immunochemotherapy. *Nat. Nanotechnol.* **18**, 193–204 (2023).
- Chen, X. et al. RNA interference-based therapy and its delivery systems. *Cancer Metast. Rev.* **37**, 107–124 (2018).
- Kanasty, R., Dorkin, J. R., Vegas, A. & Anderson, D. Delivery materials for siRNA therapeutics. *Nat. Mater.* **12**, 967–977 (2013).
- Kim, B., Park, J. H. & Sailor, M. J. Rekindling RNAi therapy: materials design requirements for in vivo siRNA delivery. *Adv. Mater.* **31**, e1903637 (2019).
- Jiang, X. et al. Oral delivery of nucleic acid therapeutics: challenges, strategies, and opportunities. *Drug Discov. Today* **28**, 103507 (2023).
- Liang, J. et al. Sphk2 RNAi nanoparticles suppress tumor growth via downregulating cancer cell derived exosomal microRNA. *J. Control. Release* **286**, 348–357 (2018).
- Zhou, X. et al. Tumour-derived extracellular vesicle membrane hybrid lipid nanovesicles enhance siRNA delivery by tumour-homing and intracellular freeway transportation. *J. Extracell. Vesicles* **11**, e12198 (2022).
- Zhuang, J. et al. Targeted gene silencing in vivo by platelet membrane-coated metal-organic framework nanoparticles. *Sci. Adv.* **6**, eaaz6108 (2020).
- Dammes, N. et al. Conformation-sensitive targeting of lipid nanoparticles for RNA therapeutics. *Nat. Nanotechnol.* **16**, 1030–1038 (2021).
- Blaby-Haas, C. E. & Merchant, S. S. Lysosome-related organelles as mediators of metal homeostasis. *J. Biol. Chem.* **289**, 28129–28136 (2014).
- Uddin, N., Binzel, D. W., Shu, D., Fu, T.-M. & Guo, P. Targeted delivery of RNAi to cancer cells using RNA-ligand displaying exosome. *Acta. Pharm. Sin. B* **13**, 1383–1399 (2023).
- Han, K. et al. A tumor targeted chimeric peptide for synergistic endosomal escape and therapy by dual-stage light manipulation. *Adv. Funct. Mater.* **25**, 1248–1257 (2015).
- Wittrup, A. et al. Visualizing lipid-formulated siRNA release from endosomes and target gene knockdown. *Nat. Biotechnol.* **33**, 870–876 (2015).
- Gilleron, J. et al. Image-based analysis of lipid nanoparticle-mediated siRNA delivery, intracellular trafficking and endosomal escape. *Nat. Biotechnol.* **31**, 638–646 (2013).
- Miller, J. B. & Siegwart, D. J. Design of synthetic materials for intracellular delivery of RNAs: from siRNA-mediated gene silencing to CRISPR/Cas gene editing. *Nano Res.* **11**, 5310–5337 (2018).
- Selby, L. I., Cortez-Jugo, C. M., Such, G. K. & Johnston, A. P. R. Nanoescapology: progress toward understanding the endosomal escape of polymeric nanoparticles. *Wiley Interdiscip. Rev. Nanomed. Nanobiotechnol.* **9**, e1452 (2017).
- Zhang, Y. et al. An antigen self-assembled and dendritic cell-targeted nanovaccine for enhanced immunity against cancer. *Acta. Pharm. Sin. B* **13**, 3518–3534 (2023).
- Kamerkar, S. et al. Exosomes facilitate therapeutic targeting of oncogenic KRAS in pancreatic cancer. *Nature* **546**, 498–503 (2017).
- Herrmann, I. K., Wood, M. J. A. & Fuhrmann, G. Extracellular vesicles as a next-generation drug delivery platform. *Nat. Nanotechnol.* **16**, 748–759 (2021).
- Kalluri, R. & LeBleu, V. S. The biology, function, and biomedical applications of exosomes. *Science* **367**, eaau6977 (2020).
- Mathieu, M., Martin-Jaular, L., Lavieu, G. & Théry, C. Specificities of secretion and uptake of exosomes and other extracellular vesicles for cell-to-cell communication. *Nat. Cell Biol.* **21**, 9–17 (2019).
- Mulcahy, L. A., Pink, R. C. & Carter, D. R. Routes and mechanisms of extracellular vesicle uptake. *J. Extracell. Vesicles* **3**, 24641 (2014).
- Tian, T. et al. Exosome uptake through clathrin-mediated endocytosis and macropinocytosis and mediating miR-21 delivery. *J. Biol. Chem.* **289**, 22258–22267 (2014).
- Cui, L. et al. Vesicle trafficking and vesicle fusion: mechanisms, biological functions, and their implications for potential disease therapy. *Mol. Biomed.* **3**, 29 (2022).
- Hindi, S. M. et al. Enveloped viruses pseudotyped with mammalian myogenic cell fusogens target skeletal muscle for gene delivery. *Cell* **186**, 2062–2077.e17 (2023).

28. Ji, X. et al. In situ cell membrane fusion for engineered tumor cells by worm-like nanocell mimics. *ACS Nano* **14**, 7462–7474 (2020).
29. Chen, P. et al. A plant-derived natural photosynthetic system for improving cell anabolism. *Nature* **612**, 546–554 (2022).
30. Ho, N. T. et al. Membrane fusion and drug delivery with carbon nanotube porins. *Proc. Natl Acad. Sci. USA* **118**, e2016974118 (2021).
31. Zheng, Z., Li, Z., Xu, C., Guo, B. & Guo, P. Folate-displaying exosome mediated cytosolic delivery of siRNA avoiding endosome trapping. *J. Control. Release* **311–312**, 43–49 (2019).
32. Sanders, D. W. et al. SARS-CoV-2 requires cholesterol for viral entry and pathological syncytia formation. *eLife* **10**, e65962 (2021).
33. Wang, C. et al. Different regions of synaptic vesicle membrane regulate VAMP2 conformation for the SNARE assembly. *Nat. Commun.* **11**, 1531 (2020).
34. Nakato, M. et al. ABCA13 dysfunction associated with psychiatric disorders causes impaired cholesterol trafficking. *J. Biol. Chem.* **296**, 100166 (2021).
35. Allen, J. A., Halverson-Tamboli, R. A. & Rasenick, M. M. Lipid raft microdomains and neurotransmitter signalling. *Nat. Rev. Neurosci.* **8**, 128–140 (2007).
36. Linetti, A. et al. Cholesterol reduction impairs exocytosis of synaptic vesicles. *J. Cell Sci.* **123**, 595–605 (2010).
37. Lötvall, J. et al. Minimal experimental requirements for definition of extracellular vesicles and their functions: a position statement from the International Society for Extracellular Vesicles. *J. Extracell. Vesicles* **3**, 26913 (2014).
38. Düzgüneş, N. & Nir, S. Mechanisms and kinetics of liposome-cell interactions. *Adv. Drug Deliv. Rev.* **40**, 3–18 (1999).
39. Kong, L., Askes, S. H. C., Bonnet, S., Kros, A. & Campbell, F. Temporal control of membrane fusion through photolabile PEGylation of liposome membranes. *Angew. Chem. Int. Ed.* **55**, 1396–1400 (2016).
40. Skotland, T., Hessvik, N. P., Sandvig, K. & Llorente, A. Exosomal lipid composition and the role of ether lipids and phosphoinositides in exosome biology. *J. Lipid Res.* **60**, 9–18 (2019).

Publisher's note Springer Nature remains neutral with regard to jurisdictional claims in published maps and institutional affiliations.

Springer Nature or its licensor (e.g. a society or other partner) holds exclusive rights to this article under a publishing agreement with the author(s) or other rightsholder(s); author self-archiving of the accepted manuscript version of this article is solely governed by the terms of such publishing agreement and applicable law.

© The Author(s), under exclusive licence to Springer Nature Limited 2024

Methods

Experimental reagents

Fresh bovine milk was obtained from a local grocery store. Me β CD was purchased from Maclean Biochemical Technology. The Amplex Red cholesterol assay kit was obtained from Invitrogen (Thermo Fisher). The following fluorescent dyes were used: 3,3'-diiodoacetyl-oxacarbocyanine perchlorate (DiO), 1,1'-diiodoacetyl-3,3',3'-tetramethylindocarbocyanine perchlorate (DiI) and 2-(4-aminophenyl)-6-indolecarbamidine dihydrochloride (DAPI). The radioimmunoprecipitation assay (RIPA) buffer, ethylene diamine tetraacetic acid (EDTA), protease inhibitor cocktail and bicinchoninic acid (BCA) protein assay kit were purchased from Meilun Biotechnology. Anti-LAMP2 antibody and anti-calnexin antibody were obtained from Abcam. Goat anti-rabbit IgG-horseradish peroxidase (HRP) and Alexa Fluor 647 goat anti-rabbit IgG (H + L) were sourced from Yeasen Biotechnology. All other chemicals used in the experiment were of analytical grade and purchased from Sinopharm Chemical Reagent. The sequences of siPLK1 were sense strand, 5'-UGAAGAAGAUACCCUCCUUAdTdT-3', antisense strand, 5'-UAAGGAGGGUGAUCUUCUUCAdTdT-3' purchased from Sangon Biotech.

Cell and animal care

Cell lines were purchased from Cell Bank, Shanghai Institute of Biochemical Cell, Chinese Academy of Sciences. HCT116-LUC cells were purchased from IMMOCELL. HCT116 cells and SK-OV-3 cells were cultured in McCoy's 5A medium; NCM460 cells, HepG2 cells, HeLa cells, 293T cells and CT26 cells were cultured in DMEM medium; 4T1 cells and HT22 cells were cultured in RPMI 1640, all medium supplemented with 1% penicillin-streptomycin and 10% FBS. Cells were maintained at 37 °C in a 5% CO₂ atmosphere. BALB/c nude mice were obtained from the Animal Experiments Center of Shanghai Institute of Materia Medica, Chinese Academy of Sciences. The *in vivo* experiment was conducted on 4- to 5-week-old male BALB/c nude mice, following the guidelines of the Institutional Animal Care (IACUC code 2023-02-GY-69). Mice were housed at 20–25 °C, with a 12 h light/dark cycle, 40–70% humidity and provided with water and standard rodent chow *ad libitum*. The maximum tumour diameter approved was 15 mm in any direction. All animal procedures complied with the Guide for the Care and Use of Laboratory Animals.

MD simulations

We used CGMD simulations to study the interactions between cell membranes and exosomes⁴¹. The simulations were performed with the GROMACS 2021.3 package using the dry Martini CG force field. The dry Martini model assumes a 4-to-1 mapping and solvent effects are implicitly included, reducing the number of particles in the simulation and significantly speeding up the computation time. This is particularly beneficial for studying phenomena where solvent effects are secondary or can be effectively parameterized, such as specific lipid-lipid or lipid-protein interactions within membranes.

Our choice of the dry Martini model was driven by its computational efficiency and proven accuracy in reproducing the qualitative behaviour of membranes containing cholesterol. We recognize that while the dry Martini force field offers significant advantages in terms of computational efficiency, it may not capture every nuance of cholesterol behaviour with the same level of detail as an all-atom or more detailed CG model. However, for the scope of our study of membrane fusion, the dry Martini model offers a balanced approach that provides insightful results that are both computationally feasible and relevant to the biological phenomena under investigation.

Isolation of MEs

Fresh milk samples were subjected to a centrifugation process at 2,500 × *g* and 4 °C for 30 min to separate the cells and cellular debris, resulting in a pellet. The defatted samples were then treated with 30 mM EDTA and incubated at 37 °C for 1 h to chelate the casein-calcium

complex. Subsequently, the mixture was subjected to successive ultracentrifugation steps at 2,500 × *g* and 12,000 × *g* for 1 h each, with the supernatant recovered and the pellet discarded between steps. This process effectively removed protein aggregates and larger contaminating vesicles. The supernatant was collected, filtered through 0.22 μm syringe filters and further subjected to ultracentrifugation at 140,000 × *g* for 1 h to pellet the milk extracellular vesicles. The resulting pellet containing the MEs was resuspended in PBS, and a final washing step was performed by ultracentrifugation at 100,000 × *g* for 1 h at 4 °C. The native MEs pellet was then resuspended in 0.5 ml of PBS and stored at –80 °C for further use.

Purification of MEs

The method was adapted from previous reports⁴². A discontinuous iodixanol gradient consisting of 40% (w/v), 20% (w/v), 10% (w/v) and 5% (w/v) solutions of iodixanol was prepared by diluting a stock solution of OptiPrep (60% (w/v) aqueous iodixanol) in 0.25 M sucrose/10 mM tris, pH 7.5. The fractions were layered with MEs isolated by differential centrifugation coupled with ultracentrifugation, resuspended in the Opti-Prep solution and overlaid onto the top layer. A control tube consisting of 3 ml of each 40%, 20%, 10% and 5% solutions was also prepared. The tubes were subjected to ultracentrifugation at 100,000 × *g* for 18 h at 4 °C. MEs were then washed with 1 ml of PBS and the supernatant was removed with successive ultracentrifugation at 100,000 × *g* for 1 h at 4 °C and resuspended before being stored at –80 °C.

Modulation of cholesterol levels in milk exosomes

The depletion of cholesterol in the milk exosome membrane was adapted from previous reports⁴³. In brief, Me β CD was added to 1 mg of MEs to achieve final concentrations of 2 mM or 4 mM, respectively. The sample was then incubated at 37 °C for 2 h to facilitate cholesterol removal. Following the incubation period, the samples were subjected to centrifugation at 140,000 × *g* for 30 min. The MEs were carefully collected from the resulting pellets and subsequently resuspended in PBS for further experimentation. The enrichment of membrane cholesterol was carried out following an established protocol⁴⁴. Initially, cholesterol was dissolved in chloroform at a concentration of 10 mg ml⁻¹. The samples were then subjected to spin evaporation to remove the chloroform and form a dry cholesterol film. To enrich the milk exosome membrane with cholesterol, 2 ml of 0.5 mg ml⁻¹ MEs was added to rehydrate 100 μg or 220 μg of the dry cholesterol film, respectively. The samples were allowed to rehydrate for 30 min. After rehydration, the samples were sonicated using an ultrasonic cell crusher for a minimum of 5 min. Subsequently, the samples were subjected to centrifugation at 140,000 × *g* for 30 min. The MEs were collected from the precipitate and resuspended in PBS. Finally, the cholesterol content in each sample was quantified using the Amplex Red cholesterol assay kit, following the recommended protocol provided by the manufacturer.

Exosomes characterization

The size and zeta potential of engineered exosomes suspended in PBS were measured using a Zetasizer (Nano ZS, Malvern Instruments). Exosome morphology was observed by TEM (Tecnaï G2 Spirit, FER) and cryo-TEM (TF20, FEI) with an acceleration voltage of 200 kV.

Elasticity measurement by AFM

Engineered exosomes were treated with tris-HCl for 5 min and then adhered to the surface of mica. The elasticity of these exosomes was determined at room temperature using AFM. AFM images were acquired in liquid using the PeakForce Quantitative Nanomechanical (QNM) mode on a Dimension FastScan AFM system (Bruker), using MLCT-C probes (silicon nitride tip) with nominal force constants of 0.01 N m⁻¹ and nominal radius of 20 nm. The resonant frequency of the probes was in the range of 7 kHz. All AFM images and measurements were conducted in tapping mode in a liquid medium, with a scanning

rate of 0.9 Hz. The force curves were measured using the same cantilever in shooting mode, with the Z piezo operating in a closed loop. For each measurement of the MEs, 10–15 shooting target measurements were averaged, and error estimates were determined. Young's modulus of the MEs was calculated using the Sneddon-modified Hertz model⁴⁵.

Proteomics analysis

Protein from the MEs was analysed according to a previously published protocol⁴⁶. In brief, consecutive fractions were collected for liquid chromatography tandem mass spectrometry analysis. To determine the biological and functional properties of all identified proteins, the identified protein sequences were analysed on the basis of Gene Ontology (GO) terms.

Investigating the uptake mechanism

The method was adapted from previous reports⁴⁷. To inhibit specific endocytosis pathways, HCT116 cells were preincubated with filipin, chlorpromazine or amiloride for 1 h and then washed three times with PBS, followed by an incubation with DiI-labelled MEs for 2 h. Subsequently, the cells were washed three times with PBS and collected by trypsin treatment. Then the collected cells were washed twice with PBS and collected by centrifugation (1,000 × *g* for 3 min). The fluorescence intensity in each well was quantitatively determined by flow cytometry (BD LSRFortessa). FlowJo (v.10) was used for flow cytometry analysis.

Membrane fusion of MEs

HCT116 cells were incubated in a 24-well plate. The cell membrane was labelled with DiO, and the outer membrane of the MEs was labelled with DiI. The MEs were then incubated with the HCT116 cells at 37 °C for 2 h. The samples were fixed with 4% PFA and stained with DAPI. The images were captured and analysed by CLSM. In parallel, membrane fusion was monitored by the FRET assay. HCT116 cells were incubated in a 96-well plate. Engineered MEs or liposomes were labelled with 1% fluorescent lipid NBD-PE and Rho-PE and then incubated with the HCT116 cells at 37 °C for 2 h. The final volume was 200 µl. Fusion efficiency was determined by the change in NBD fluorescence intensity before and after fusion. The fluorescence intensity of NBD was expressed as F_{∞} . The fusion efficiency was calculated by $\frac{F_n - F_0}{F_{\infty} - F_0}$, where F_0 and F_n are the fluorescence intensities before and after fusion. Furthermore, the prepared engineered MEs were fixed in anti-CD63 primary antibody (1:100 dilution) at 37 °C for 1 h. The free primary antibody was removed by ultracentrifugation and incubated in gold 5 nm-conjugated goat anti-rabbit secondary antibody (1:1,000 dilution) for 1 h. Finally, CD63-AuNP-functionalized MEs were obtained by ultracentrifugation. And then the HCT116 cells were incubated with gold nanoparticle-labelled MEs (100 µg ml⁻¹) for 2 h. Then the cells were washed twice with PBS and fixed with 2.5% glutaraldehyde at 4 °C for 2 h. After that, cells were fixed with 1% OsO₄ in 0.1 M phosphate buffer for 2 h, dehydrated with an ethanol gradient, treated with lead citrate staining and subjected to TEM analysis.

Intracellular fate of MEs

In brief, DiI-labelled MEs were added to HCT116 cells and incubated for 2 h. Then the HCT116 cells were stained with Hoechst 33342 and LysoTracker Green at 37 °C for 1 h. The colocalization signals of MEs with lysosome were imaged by CLSM. Similarly, we incubated MEs with cells expressing EGFP-labelled Rab5^{Q79L}, serving as an early endosome marker. Then the HCT116 cells were stained with Hoechst 33342 for 30 min. The colocalization signals of MEs with early endosome were imaged by CLSM.

HIS-SIM imaging

The procedure for imaging was performed by following the previous report⁴⁸. HIS-SIM was used for super-resolution imaging of the process of MEs entry. The cell membrane was labelled with DiO, and the outer

membrane of the MEs was labelled with DiI. Images were acquired using a 100×/1.5 NA oil immersion objective (Olympus). Cells were seeded in confocal dishes and maintained at 37 °C and 5% CO₂ in a humidified chamber for live SIM imaging. SIM images were collected and analysed as described previously⁴⁹.

Intracellular fate of Cy3-siRNA/MEs

In brief, Cy3-siRNA/MEs were added to HCT116 cells, which were incubated for 4 h. The HCT116 cells were stained with Hoechst 33342 and LysoTracker Green at 37 °C for 1 h. The colocalization signals of Cy3-siRNA with lysosomes were imaged by CLSM. Similarly, Cy3-siRNA/MEs were added to HCT116 cells, which were incubated for 4 h. The cells were fixed with 100% methanol (5 min), permeabilized with 0.1% Triton X-100 for 5 min and then blocked with 1% BSA/10% normal goat serum/0.3 M glycine in 0.1% PBS-Tween for 1 h. The cells were then incubated with anti-calreticulin overnight at 4 °C, followed by a further incubation at room temperature for 1 h with a goat secondary antibody to rabbit IgG (Alexa Fluor 647) at 2 µg ml⁻¹. Nuclear DNA was labelled in blue with DAPI. Afterwards, the colocalization signals of Cy3-siRNA with ER were imaged by CLSM. In parallel, HCT116 cells were incubated in a 24-well plate. Rhodamine B-loaded MEs were then incubated with the HCT116 cells at 37 °C for 4 h. The cell membrane was labelled with DiO. The samples were fixed with 4% PFA and stained with DAPI. The images were captured and analysed in 3D by CLSM.

Western blotting assay

The method was adapted from previous reports⁵⁰. HCT116 cells were seeded in six-well plates and incubated for 12 h. Various siPLK1-incorporated formulations were diluted to the final volume of 1 ml (the final concentration of siRNA is 100 nM) and then incubated with HCT116 cells for 48 h. After washing with PBS, the cells were lysed by the mixture of RIPA buffer and PMSF at the ratio of 100:1. The total proteins in each sample were quantified by a BCA protein assay kit and separated by a 10% SDS-PAGE. Afterwards, the samples were transferred to the PVDF membrane through electrophoretic blotting. Then PVDF membranes were blocked in 5% skimmed milk and incubated with antibodies against PLK1 and GAPDH. Anti-rabbit IgG (HRP-linked antibody) was used as the secondary antibody and then dosing an automatic chemiluminescence imaging system was analysed.

RT-qPCR analysis

HCT116 cells were seeded in 12-well plates and incubated for 12 h. Various siPLK1-incorporated formulations were diluted to the final volume of 500 µl (the concentration of siRNA is 100 nM) and then incubated with HCT116 cells for 48 h. Total RNAs of as-treated HCT116 cells were extracted using Trizol reagent kit. Reverse transcription of mRNA and qPCR experiments were carried out using PrimeScript RT reagent kit with gDNA Eraser and TB Green Premix Ex Taq, respectively. mRNA expression was quantified with the Applied Biosystems 7500 Fast Real-Time PCR System (ABI). The expression level of mRNA was quantified by the 2^{-ΔΔCt} (threshold cycle) method. For PLK1, the forward primer was designed as 5'-AGCCTGAGGCCCGATACTACTAC-3' and the reverse primer was designed as 5'-ATTAGGAGTCCCACACAGGGTCTTC-3'. For GAPDH, the forward primer was designed as 5'-CTGGGCTACTAGCACC-3' and the reverse primer was designed as 5'-AAGTGGTCGTTGAGGGCAATG-3'.

Cell viability

After incubation with the siPLK1-incorporated formulation for 48 h, the viability of HCT116 cells were analysed by a CCK-8 assay according to the manufacturer's instruction.

Cell apoptosis

HCT116 cells were seeded in 12-well plates and incubated for 12 h. Various siPLK1-incorporated formulations were diluted to the final

volume of 500 μl (the concentration of siRNA is 100 nM) and then incubated with HCT116 cells for 48 h. After executing the annexin V-FITC/propidium iodide (PI) staining by annexin V-FITC apoptosis detection kit, the apoptosis analysis was conducted by flow cytometry.

Cell cycle analysis

HCT116 cells were seeded in 12-well plates and incubated for 12 h. Various siPLK1-incorporated formulations were diluted to the final volume of 500 μl (the concentration of siRNA is 100 nM) and then incubated with HCT116 cells. After the cells were incubated for 48 h, these cells were collected and washed three times with PBS. Then cells were centrifuged (500 $\times g$, 3 min), the supernatant was discarded, and the cell pellet was fixed in 70% ethanol at 4 $^{\circ}\text{C}$ for 24 h. Before analysis, the cells were washed once in PBS and stained with 500 μl PI/RNase for 15 min in the dark at room temperature. The cell cycle analysis was conducted by flow cytometry.

Gene silencing performance of MEs/siRNA formulation in vivo

The orthotopic colorectal cancer model was developed based on the literature⁵¹. Male BALB/c nude mice (4–5 weeks old) were anaesthetized by Zoletil 50. The abdomen was sterilized with alcohol swabs. A median incision was then made through the lower ventral abdominal, and the cecum was exteriorized. A suspension of 3×10^6 HCT116-LUC cells in 50 μl serum-free 5A medium containing Matrigel was injected into the cecal wall. The cecum was then returned to the peritoneal cavity, and the peritoneum and skin were closed with suture, respectively. The tumour formation and growth were monitored using the PE IVIS spectrum imaging system.

Ten days after orthotopic tumour cell inoculation, the tumour-bearing mice were treated with PBS (control), 5%Chol/siPLK1, 18%Chol/siPLK1, 30%Chol/siPLK1 and LNP/siPLK1 at siRNA dose of 0.1 mg kg^{-1} via oral gavage every consecutive day for 14 days. Each group included five mice. The tumour burden was monitored weekly using bioluminescence imaging and the body weight was recorded throughout the study. The major organs including heart, liver, spleen, lung and kidney were collected for H&E histological assay for toxicity evaluation.

To establish colorectal cancer xenograft tumour model, about 20 g of male BALB/c nude mice were selected and subcutaneously inoculated with HCT116 cells (2×10^6 cells per mouse). After the tumour grew to about 6 mm in diameter, 100 μl of siPLK1-incorporated formulations was intravenously injected via tail vein every 3 days (the siRNA dose used for in vivo studies is about 0.1 mg kg^{-1}). After 3-week treatment, the tumour was collected and analysed by histological section.

Statistics and reproducibility

All experiments were performed with at least three biological replicates with similar results. Representative TEM images, AFM images, cryo-TEM images and microscopy images that came from at least three independent experiments are shown. All values are expressed as mean \pm s.d. Statistical significance was determined using ordinary one-way analysis of variance (ANOVA) or three-way ANOVA with Dunnett's multiple comparisons. Data analysis was performed using GraphPad Prism 8.0 software and *P* values less than 0.05 were considered statistically significant (**P* < 0.05, ***P* < 0.01, ****P* < 0.001, *****P* < 0.0001, NS, not significant). Detailed method information and event numbers are provided in the respective figure legends.

Reporting summary

Further information on research design is available in the Nature Portfolio Reporting Summary linked to this article.

Data availability

All data supporting the findings of this study are included in the article and the Supplementary Information. There are no data from third-party

or publicly available datasets. All data generated as part of this study are available from the corresponding author upon reasonable request. Source data are provided with this paper.

References

1. Arnarez, C. et al. Dry Martini, a coarse-grained force field for lipid membrane simulations with implicit solvent. *J. Chem. Theory Comput.* **11**, 260–275 (2015).
2. Samuel, M. et al. Oral administration of bovine milk-derived extracellular vesicles induces senescence in the primary tumor but accelerates cancer metastasis. *Nat. Commun.* **12**, 3950 (2021).
3. Ziolkowski, W. et al. Methyl-beta-cyclodextrin induces mitochondrial cholesterol depletion and alters the mitochondrial structure and bioenergetics. *FEBS Lett.* **584**, 4606–4610 (2010).
4. Chabanel, A. et al. Influence of cholesterol content on red cell membrane viscoelasticity and fluidity. *Biophys. J.* **44**, 171–176 (1983).
5. Li, M. et al. Nanoscale imaging and mechanical analysis of Fc receptor-mediated macrophage phagocytosis against cancer cells. *Langmuir* **30**, 1609–1621 (2014).
6. Zheng, D. W. et al. Hierarchical micro-/nanostructures from human hair for biomedical applications. *Adv. Mater.* **30**, e1800836 (2018).
7. Qiu, Y. et al. Yolk-shell cationic liposomes overcome mucus and epithelial barriers for enhanced oral drug delivery. *Giant* **17**, 100221 (2024).
8. Wang, X. et al. Efficient base editing in methylated regions with a human APOBEC3A-Cas9 fusion. *Nat. Biotechnol.* **36**, 946–949 (2018).
9. Zhao, E. et al. Spatial transcriptomics at subspot resolution with BayesSpace. *Nat. Biotechnol.* **39**, 1375–1384 (2021).
10. Xue, C. et al. Programmably tiling rigidified DNA brick on gold nanoparticle as multi-functional shell for cancer-targeted delivery of siRNAs. *Nat. Commun.* **12**, 2928 (2021).
11. Liu, H.-J. et al. Integrated combination treatment using a 'smart' chemotherapy and microRNA delivery system improves outcomes in an orthotopic colorectal cancer model. *Adv. Funct. Mater.* **28**, 1801118 (2018).

Acknowledgements

We sincerely appreciate the financial support from the National Science Fund of Distinguished Young Scholars (82025032), the National Key Research and Development Program of China (2022YFA1203200), the National Natural Science Foundation of China (82073773), the Young Elite Scientists Sponsorship Program by CAST (2022QNRCC001), the Key Research Program of Chinese Academy of Sciences (ZDBS-ZRKJZ-TLC005), the 'Open Competition to Select the Best Candidates' Key Technology Program for Nucleic Acid Drugs of NCTIB (NCTIB2022HS01006), the Shanghai Action Plan for Science, Technology and Innovation (23HC1401200) and the Shanghai Institute of Materia Medica, Chinese Academy of Sciences (SIMMO220232001). We thank the staff members of the Integrated Laser Microscopy System, the Electron Microscopy System, the Molecular Imaging System and the Large-scale Protein Preparation System at the National Facility for Protein Science in Shanghai (NFPS), Shanghai Advanced Research Institute, Chinese Academy of Sciences, China, for sample preparation, data collection and analysis. The MD simulations were performed on BSCC-A6 at the Beijing Super Cloud Computing Center. We are grateful to G. Li, Y. Yu, F. Gong and F. Liu for cryo-TEM data collection, cell imaging and AFM data collection, respectively.

Author contributions

M.Y., G.H., Y.G., Y.Z. and Z.L. planned and executed the experiments, analysed the data and were involved in discussions of the data. M.Y., G.H., Y.Z., Z.L. and Z. Zhu wrote the paper. Y.Z., Z.L., Z. Zhu,

J.W., X.L., Z. Zhang, C.G., B.W. and D.N. performed the experiments. All authors critically reviewed and approved the paper.

Competing interests

The authors declare no competing interests.

Additional information

Supplementary information The online version contains supplementary material available at <https://doi.org/10.1038/s41565-024-01785-0>.

Correspondence and requests for materials should be addressed to Yong Gan, Guoqing Hu or Miaorong Yu.

Peer review information *Nature Nanotechnology* thanks the anonymous reviewers for their contribution to the peer review of this work.

Reprints and permissions information is available at www.nature.com/reprints.

Reporting Summary

Nature Portfolio wishes to improve the reproducibility of the work that we publish. This form provides structure for consistency and transparency in reporting. For further information on Nature Portfolio policies, see our [Editorial Policies](#) and the [Editorial Policy Checklist](#).

Statistics

For all statistical analyses, confirm that the following items are present in the figure legend, table legend, main text, or Methods section.

n/a Confirmed

- The exact sample size (n) for each experimental group/condition, given as a discrete number and unit of measurement
- A statement on whether measurements were taken from distinct samples or whether the same sample was measured repeatedly
- The statistical test(s) used AND whether they are one- or two-sided
Only common tests should be described solely by name; describe more complex techniques in the Methods section.
- A description of all covariates tested
- A description of any assumptions or corrections, such as tests of normality and adjustment for multiple comparisons
- A full description of the statistical parameters including central tendency (e.g. means) or other basic estimates (e.g. regression coefficient) AND variation (e.g. standard deviation) or associated estimates of uncertainty (e.g. confidence intervals)
- For null hypothesis testing, the test statistic (e.g. F , t , r) with confidence intervals, effect sizes, degrees of freedom and P value noted
Give P values as exact values whenever suitable.
- For Bayesian analysis, information on the choice of priors and Markov chain Monte Carlo settings
- For hierarchical and complex designs, identification of the appropriate level for tests and full reporting of outcomes
- Estimates of effect sizes (e.g. Cohen's d , Pearson's r), indicating how they were calculated

Our web collection on [statistics for biologists](#) contains articles on many of the points above.

Software and code

Policy information about [availability of computer code](#)

Data collection

Coarse-grained molecular dynamics simulations (CGMD): GROMACS 2021.3 package; Size and zeta potential data: Malvern Zetasizer Nano ZS; Cholesterol content: Amplex Red cholesterol assay; TEM images: Tecnai G2 Spirit 120kV; Atomic force microscopy (AFM) images: FastScan Bio atomic force microscopy; Cryo-TEM images: FEI Tecnai G2 F20; Proteomic analysis: Q Exactive HF; Confocal laser scanning microscopy (CLSM) images: Leica TCS SP8 and Olympus FV1000; Flow Cytometer: BD LSR Fortessa; NIR-II images: MARS NIR-II in vivo imaging system; Histological section images: NanoZoomer 2.0 HT; Fluorescence resonance energy transfer (FRET) data: SYNERGY H1 microplate reader.

Data analysis

Visual Molecular Dynamics (VMD) 1.9.4; Origin 2019b; Graphpad Prism 8.0; MaxQuant(1.6.5.0); Image J Fiji 1.53c; Leica Application Suite X (LAS X); Chemiscope 6100 Touch; Olympus FV10-ASW 4.2 Viewer; Flowjo V10; NanoScope Analysis 1.7; Adobe Illustrator 2020; NDP.view2 (U12388-01).

For manuscripts utilizing custom algorithms or software that are central to the research but not yet described in published literature, software must be made available to editors and reviewers. We strongly encourage code deposition in a community repository (e.g. GitHub). See the Nature Portfolio [guidelines for submitting code & software](#) for further information.

Data

Policy information about [availability of data](#)

All manuscripts must include a [data availability statement](#). This statement should provide the following information, where applicable:

- Accession codes, unique identifiers, or web links for publicly available datasets
- A description of any restrictions on data availability
- For clinical datasets or third party data, please ensure that the statement adheres to our [policy](#)

All data supporting the findings of this study are included in the Article and the Supplementary Information. There are no data from third-party or publicly available datasets. All data generated as part of this study are available from the corresponding author upon reasonable request. Source data are provided with this paper.

Research involving human participants, their data, or biological material

Policy information about studies with [human participants or human data](#). See also policy information about [sex, gender \(identity/presentation\), and sexual orientation](#) and [race, ethnicity and racism](#).

Reporting on sex and gender	This study involved no human research.
Reporting on race, ethnicity, or other socially relevant groupings	This study involved no human research.
Population characteristics	This study involved no human research.
Recruitment	This study involved no human research.
Ethics oversight	This study involved no human research.

Note that full information on the approval of the study protocol must also be provided in the manuscript.

Field-specific reporting

Please select the one below that is the best fit for your research. If you are not sure, read the appropriate sections before making your selection.

- Life sciences Behavioural & social sciences Ecological, evolutionary & environmental sciences

For a reference copy of the document with all sections, see [nature.com/documents/nr-reporting-summary-flat.pdf](https://www.nature.com/documents/nr-reporting-summary-flat.pdf)

Life sciences study design

All studies must disclose on these points even when the disclosure is negative.

Sample size	Sample sizes were determined based on previous studies conducted using similar setups, without the need for additional statistical. To ensure statistical significance, all in vitro experiments described in this paper were performed with $n > 3$. A minimum of 3 independent repeats was required to evaluate statistical significance (Nat. Biomed. 2019, 3, 729-740; Nat. Commun. 2021, 12, 1138; Nat. Commun. 2021, 12, 2928); The in vivo studies were performed with $n = 5$ mice per group to achieve statistical validity (Nature. 2009, 458, 1180-1184; Adv. Funct. Mater. 2018, 28, 1801118). Details regarding sample sizes and statistical tests of all experiments are provided in the methods section and figure captions.
Data exclusions	We did not exclude any data.
Replication	The experiments were repeated for 3 times in vitro, and the results were consistent with each other. For the in vivo study, each group contained 5 mice. Numbers of replicated events were detailed in the relevant figure legends.
Randomization	All samples and animals were randomly assigned into groups.
Blinding	We were blinded to group allocation during all of data collection and analysis.

Reporting for specific materials, systems and methods

We require information from authors about some types of materials, experimental systems and methods used in many studies. Here, indicate whether each material, system or method listed is relevant to your study. If you are not sure if a list item applies to your research, read the appropriate section before selecting a response.

Materials & experimental systems

n/a	Involved in the study
<input type="checkbox"/>	<input checked="" type="checkbox"/> Antibodies
<input type="checkbox"/>	<input checked="" type="checkbox"/> Eukaryotic cell lines
<input checked="" type="checkbox"/>	<input type="checkbox"/> Palaeontology and archaeology
<input type="checkbox"/>	<input checked="" type="checkbox"/> Animals and other organisms
<input checked="" type="checkbox"/>	<input type="checkbox"/> Clinical data
<input checked="" type="checkbox"/>	<input type="checkbox"/> Dual use research of concern
<input checked="" type="checkbox"/>	<input type="checkbox"/> Plants

Methods

n/a	Involved in the study
<input checked="" type="checkbox"/>	<input type="checkbox"/> ChIP-seq
<input type="checkbox"/>	<input checked="" type="checkbox"/> Flow cytometry
<input checked="" type="checkbox"/>	<input type="checkbox"/> MRI-based neuroimaging

Antibodies

Antibodies used

All the antibodies were diluted and used following the supplier's protocols.
 Anti-PLK1: polo-like kinase 1 (Wanleibio, cat. WL04381 (1:750 dilution))
 Anti-GAPDH: Glyceraldehyde-3-phosphate dehydrogenase (Yeasen Biotechnology, cat. 30202ES40(1:5000 dilution))
 Anti-Calreticulin antibody [EPR3924] (Abcam, cat. ab92516 (1:500))
 Anti-LAMP2 antibody [GL2A7] (Abcam, cat. ab13524 (1:1000))
 Alexa Fluor 647 Goat Anti-Rabbit IgG(H+L): (Yeasen Biotechnology, cat. 33113ES60 (1:200 dilution))
 Anti-TSG 101 (C-2): (Santa Cruz Biotechnology, cat. I1721 (1:200 dilution))
 Anti-Calnexin (AF18): (Santa Cruz Biotechnology, cat. A2722 (1:200 dilution))
 Anti-CD63: LAMP-3, lysosome-associated membrane protein-3 (Wanleibio, cat. WL02549 (1:1500 dilution))
 Anti-Alix: (Wanleibio, cat. WL03063 (1:1500 dilution))
 HRP-labeled Goat Anti-Rabbit IgG(H+L): (Beyotime, cat. A0208 (1:1000 dilution))
 Gold 5 nm-conjugated goat anti-rabbit secondary antibody: (Solarbio, cat. K0034G (1:1000 dilution))

Validation

All the primary antibodies are well-recognized clones, as noted in many publications, and are commercially available and validated by the manufacturers, as indicated on their websites. These antibodies are further validated and routinely used in our lab, with good reproducibility.

1. Anti-PLK1 has been validated for WB analysis. Reactivity with human, mouse and rat were test. <https://admin.biodog.cn/uploads/File/pdf/WL04381.pdf>
2. Anti-GAPDH has been validated for WB analysis. Reactivity with human, mouse and rat were test. <https://www.yeasen.com/products/detail/882>
3. Anti-Calreticulin antibody has been validated for immunofluorescence analysis. Reactivity with human, mouse and rat were test. <https://www.abcam.cn/products/primary-antibodies/calreticulin-antibody-epr3924-er-marker-ab92516.html>
4. Anti-LAMP2 antibody has been validated for immunofluorescence analysis. Reactivity with human, mouse and rat were test. <https://www.abcam.cn/products/primary-antibodies/lamp2-antibody-gl2a7-ab13524.html>
5. Alexa Fluor 647 Goat Anti-Rabbit IgG(H+L) immunofluorescence analysis. Reactivity with rabbit was test. <https://www.yeasen.com/products/detail/369>
6. Anti-TSG 101 (C-2) has been validated for WB analysis. Reactivity with human, mouse and rat were test. <https://www.scbt.com/p/tsg-101-antibody-c-2>
7. Anti-Calnexin (AF18) has been validated for WB analysis. Reactivity with human, mouse and rat were test. <https://www.scbt.com/zh/p/calnexin-antibody-af18>
8. Anti-CD63 has been validated for WB analysis. Reactivity with human, mouse and rat were test. <https://admin.biodog.cn/uploads/File/202310/5aa23a194a1afca2e11209b3287fc7f7.pdf>
9. Anti-Alix has been validated for WB analysis. Reactivity with human, mouse and rat were test. <https://admin.biodog.cn/uploads/File/202407/e63200b2e792397d3a760219504f1373.pdf>
10. HRP-labeled Goat Anti-Rabbit IgG(H+L) has been validated for WB analysis. Reactivity with rabbit was test. <https://www.beyotime.com/product/A0208.htm>
11. Gold 5 nm-conjugated goat anti-rabbit secondary antibody has been validated for TEM analysis. Reactivity with rabbit was test. <https://www.solarbio.com/goodsInfo?id=222132>

Eukaryotic cell lines

Policy information about [cell lines and Sex and Gender in Research](#)

Cell line source(s)

HCT116 cells, HepG2 cells, SK-OV-3 cells, HeLa cells; 4T1 cells, 293T cells, HT22 cells, CT26 cells and NCM460 cells were purchased from Cell bank, Shanghai Institute of Biochemical Cell, Chinese Academy of Sciences. HCT116-LUC cells were purchased from IMMOCELL (Xiamen, Fujian, China).

Authentication

The cell lines purchased from Cell bank, Shanghai Institute of Biochemical Cell, Chinese Academy of Sciences and authenticated by the vendors. In all related studies, cell lines with a low passage number were used.

Mycoplasma contamination

All cell lines were confirmed to be free of mycoplasma.

Commonly misidentified lines
(See [ICLAC](#) register)

No commonly misidentified cell lines were used.

Animals and other research organisms

Policy information about [studies involving animals](#); [ARRIVE guidelines](#) recommended for reporting animal research, and [Sex and Gender in Research](#)

Laboratory animals	BALB/c nude mice were obtained from the Animal Experiments Center of Shanghai Institute of Materia Medica, Chinese Academy of Sciences. The in vivo experiment was performed on 4- to 5-week-old male BALB/c nude mice following the guidelines of the Institutional Animal Care (IACUC code: 2023-02-GY-69). Mice were housed in a controlled environment at 20-25 °C with a 12h light/dark cycle and 40-70% humidity. They were provided free access to water and standard rodent chow. All animal experimental operations were in accordance with the specifications of the Guide for the Care and Use of Laboratory Animals.
Wild animals	The study did not involve wild animals.
Reporting on sex	The study used only male rats. The sex-based analyses were not considered, as sex had negligible effects on the results.
Field-collected samples	The study did not involve samples collected from the field.
Ethics oversight	All animal experiments were conducted following the relevant requirements of the Institutional Animal Care and Use Committee (IACUC) guidelines of the Shanghai Institute of Materia Medica, Chinese Academy of Sciences (IACUC code: 2023-02-GY-69).

Note that full information on the approval of the study protocol must also be provided in the manuscript.

Plants

Seed stocks	<i>Report on the source of all seed stocks or other plant material used. If applicable, state the seed stock centre and catalogue number. If plant specimens were collected from the field, describe the collection location, date and sampling procedures.</i>
Novel plant genotypes	<i>Describe the methods by which all novel plant genotypes were produced. This includes those generated by transgenic approaches, gene editing, chemical/radiation-based mutagenesis and hybridization. For transgenic lines, describe the transformation method, the number of independent lines analyzed and the generation upon which experiments were performed. For gene-edited lines, describe the editor used, the endogenous sequence targeted for editing, the targeting guide RNA sequence (if applicable) and how the editor was applied.</i>
Authentication	<i>Describe any authentication procedures for each seed stock used or novel genotype generated. Describe any experiments used to assess the effect of a mutation and, where applicable, how potential secondary effects (e.g. second site T-DNA insertions, mosaicism, off-target gene editing) were examined.</i>

Flow Cytometry

Plots

Confirm that:

- The axis labels state the marker and fluorochrome used (e.g. CD4-FITC).
- The axis scales are clearly visible. Include numbers along axes only for bottom left plot of group (a 'group' is an analysis of identical markers).
- All plots are contour plots with outliers or pseudocolor plots.
- A numerical value for number of cells or percentage (with statistics) is provided.

Methodology

Sample preparation	Samples were prepared according to methods listed in "Flow cytometry" section.
Instrument	BD LSR Fortessa
Software	Flowjo V10
Cell population abundance	The absolute cells >= 10,000 were collected and analyzed
Gating strategy	Preliminary FSC-A/SSC-A gates were used on morphology and FSC-A/FSC-H for singlets.

- Tick this box to confirm that a figure exemplifying the gating strategy is provided in the Supplementary Information.